

Optoacoustic mesoscopy for biomedicine

Murad Omar^{1,2}, Juan Aguirre^{1,2} and Vasilis Ntziachristos^{1,2*}

Fuelled by innovation, optical microscopy plays a critical role in the life sciences and medicine, from basic discovery to clinical diagnostics. However, optical microscopy is limited by typical penetration depths of a few hundred micrometres for *in vivo* interrogations in the visible spectrum. Optoacoustic microscopy complements optical microscopy by imaging the absorption of light, but it is similarly limited by penetration depth. In this Review, we summarize progress in the development and applicability of optoacoustic mesoscopy (OPAM); that is, optoacoustic imaging with acoustic resolution and wide-bandwidth ultrasound detection. OPAM extends the capabilities of optical imaging beyond the depths accessible to optical and optoacoustic microscopy, and thus enables new applications. We explain the operational principles of OPAM, its placement as a bridge between optoacoustic microscopy and optoacoustic macroscopy, and its performance in the label-free visualization of tissue pathophysiology, such as inflammation, oxygenation, vascularization and angiogenesis. We also review emerging applications of OPAM in clinical and biological imaging.

The tissue-penetration depth of optical microscopy depends primarily on the amount of photon scatter. Intravital fluorescence microscopy (for example, confocal microscopy and multiphoton microscopy) cannot typically image beyond a few hundred micrometres in the visible spectral region, or beyond ~1–1.5 mm in the infrared region^{1–4}. Optical coherence tomography^{5–7} (OCT; developed for imaging tissue morphology), wavefront shaping, beam-profile shaping and phase control of the photon-plane wavefront^{8–11}, are being considered for improving the penetration depth of optical microscopy in the 1–2 mm range. To visualize deeper into tissues, optical-clearing methods—which chemically process a sample to make it transparent^{12–14}—can be used, but because these methods are toxic to tissue they are only appropriate for post-mortem applications. Alternatively, optical mesoscopy^{15–18} and optical macroscopy^{16,19,20} of intact tissues allow for *in vivo* imaging through several millimetres (and even centimetres) of tissue, yet at a rapidly decreasing resolution, owing to photon scatter.

First considered in the 1970s (refs. ^{21,22}), optoacoustic (or photoacoustic) imaging is a class of optical (photonic) imaging methods that is insensitive to photon scatter^{23–25}. The technique offers a radically different approach to optical imaging deep inside tissues by resolving the absorption of light on the basis of the detection of ultrasound waves rather than photons. The ultrasound waves are generated within the sample in response to the thermoelastic expansion of tissue moieties that absorbed light of transient energy. Excitation light is delivered with wide-field illumination and yields volumetric tissue excitation. Typically, the origins of the sound waves are reconstructed by using mathematical inversion, yielding an image of the distribution of light absorbers in the sample. Because image formation is governed by ultrasound diffraction, the technique is generally termed acoustic-resolution (AR) optoacoustic imaging, and achieves high-resolution optical imaging at much greater depths than optical microscopy because it is insensitive to photon scatter. Optoacoustic imaging can also be implemented by using focused light for ultrasound excitation, in analogy to illumination practices employed in intravital optical microscopy^{23,26,27}. Termed optical-resolution (OR) optoacoustic (or photoacoustic) microscopy^{27,28}, the method nevertheless obeys the laws of optical diffraction and operates within the specifications that are common to optical microscopy.

AR optoacoustic imaging can be classified in analogy to the macroscopy, mesoscopy and microscopy domains defined for optical imaging^{19,23,29–32}. Following the paradigm of optical mesoscopy^{15,16,33}, optoacoustic mesoscopy (OPAM) has been described as a bridge between optoacoustic macroscopy and optoacoustic microscopy²⁹. Although there are not hard boundaries between these imaging domains, there are characteristic technological and operational features that set the domains apart. Optoacoustic macroscopy generally aims at visualization within depths of several centimetres in tissues, for example enabling the non-invasive imaging of breast cancer^{34–36}, intestinal inflammation³⁷ and brown-fat metabolism in humans³⁸. Macroscopic implementations operate with laser pulses at tens of millijoules, and use ultrasound arrays operating at single-digit frequencies in the MHz scale, achieving resolutions in the hundreds of micrometres (Table 1). At these frequencies, whole-body animal imaging is also possible^{23,39,40}. Conversely, mesoscopy involves higher ultrasound frequencies, achieving penetration depths of a few millimetres and resolutions in the several tens of micrometres. This performance is suitable for dermatology, endoscopy and many biological-imaging applications. Single-element detectors are preferred for high-quality image performance in OPAM, but mesoscopes are also implemented with high-frequency ultrasound (HFUS) arrays in the few tens of MHz. Also, microscopy aims for visualization at resolutions of roughly the scale of cells, requiring either optical focusing or ultrasound frequencies in the upper tens to hundreds of MHz, which is also typically achieved with single-element detectors^{29,31,41}.

In this Review, we explain the principle of operation of OPAM, and summarize recent progress in technical developments and applications. We posit that bandwidth is a key driving force of imaging performance, and discuss advances in ultrawide-bandwidth (UWB) detection, which offers detailed optical-absorption images in the mesoscopic regime. Applied at a single wavelength or at multiple wavelengths, OPAM offers label-free imaging of tissue pathophysiology, which can be further complemented by the use of contrast-enhancing agents. These capabilities can bring new solutions to unmet medical-imaging needs, in particular in dermatology, endoscopy and intravascular imaging (that is, in imaging areas that require large fields of view and high-resolution imaging

¹Institute of Biological and Medical Imaging, Helmholtz Zentrum München, Munich, Germany. ²Chair of Biological Imaging, Technische Universität München, Munich, Germany. *e-mail: v.ntziachristos@tum.de

Table 1 | Typical technical and operational characteristics of state-of-the-art implementations of optoacoustic microscopy, mesoscopy and macroscopy

	OR optoacoustic microscopy	AR optoacoustic microscopy	AR optoacoustic mesoscopy	AR optoacoustic macroscopy
Image formation	Scanning	Scanning	Mathematical inversion	Mathematical inversion
Illumination	Diffraction-focused	Unfocused or moderately focused	Wide field	Wide field
Energy per pulse	<1 μJ	focused	0.01–10 mJ	>10 mJ
Repetition rate	10–500 kHz	<10 μJ	1–500 kHz	10–100 Hz
Pulse width	0.003–10 ns	10–500 kHz 0.3–10 ns	1–10 ns	20–200 ns
Detection (typical)	Single detector	Single detector	Single detector or detector array	Detector array
Bandwidth	~10–100 MHz	>~50 MHz	~10–200 MHz	<~10 MHz
Resolution ^a	Optical diffraction	Acoustic diffraction	Acoustic diffraction	Acoustic diffraction
Lateral resolution	<3 μm	<50 μm	<100 μm	100–500 μm
Axial resolution	<30 μm	<30 μm	10–100 μm	100–500 μm
Depth ^a	<1 mm	1–2 mm	0–10 mm	>10 mm
Primary limitation	Photon scatter	Ultrasound attenuation	Ultrasound attenuation	Light attenuation

^aTypical values (rather than absolute boundaries).

through several millimetres of tissue). They also advance observations in biomedical research employing animal models.

Technology advances in OPAM

Optoacoustic pressure signals $p(\mathbf{r}, t)$ (Pa) are generated inside tissues when chromophores or agents absorb light of varying intensity. Through thermoelastic expansion, the absorbed optical energy is converted to pressure waves at ultrasonic frequencies. When short light pulses (in the nanosecond range) are employed, heat and stress remain approximately confined within the absorbing tissue. In this case, the propagation of the optoacoustic wave $p(\mathbf{r}, t)$ is governed by the wave equation^{42,43}

$$\nabla^2 p(\mathbf{r}, t) - \frac{1}{v_s^2} \frac{\partial^2 p(\mathbf{r}, t)}{\partial t^2} = -\frac{\Gamma}{v_s^2} \frac{\partial H(\mathbf{r}, t)}{\partial t} \quad (1)$$

where v_s (m s⁻¹) is the speed of sound in the medium, Γ the dimensionless Grueneisen parameter, $H(\mathbf{r}, t) = \eta_{th} \times \mu_a(\mathbf{r}) \times \phi(\mathbf{r}, t)$ (W m⁻³) the deposited (absorbed) optical energy per unit volume and unit time, $\phi(\mathbf{r}, t)$ (W m⁻²) the optical fluence rate, $\mu_a(\mathbf{r})$ (1 m⁻¹) the spatially dependent absorption coefficient, and η_{th} the dimensionless heat-conversion efficiency^{42–44}. For simplicity, we assume that $\eta_{th}=1$, and that Γ is constant throughout tissue. If heat-confinement and stress-confinement conditions are fulfilled^{40,45}, then the heating function can be expressed as: $H(\mathbf{r}, t) = H_S(\mathbf{r})\delta(t)$, whereby $H_S(\mathbf{r}) = \mu_a(\mathbf{r})F(\mathbf{r})$ (J m⁻³) is the absorbed optical energy per unit volume and $F(\mathbf{r})$ (J m⁻²) the optical fluence⁴⁵. Then, equation (1) can be solved to express the pressure wave $p(\mathbf{r}, t)$ reaching a position \mathbf{r} in space as^{42,43,46}

$$p(\mathbf{r}, t) = \frac{\Gamma}{4\pi v_s^2} \frac{\partial}{\partial t} \int \frac{H_S(\mathbf{r}') \delta(t - |\mathbf{r}-\mathbf{r}'|/v_s)}{|\mathbf{r}-\mathbf{r}'|} d\mathbf{r}' \quad (2)$$

$$= \frac{1}{4\pi v_s^2} \frac{\partial}{\partial t} \int_{S'(t)} \frac{p_0(\mathbf{r}')}{|\mathbf{r}-\mathbf{r}'|} dS'(\mathbf{r}')$$

where $p_0(\mathbf{r}')$ (Pa) is the spatial distribution of the initial optoacoustic pressure, that is, $p_0(\mathbf{r}') = \Gamma \times H_S(\mathbf{r}')$. $S'(t)$ is a spherical surface centred at \mathbf{r} with radius $|\mathbf{r}-\mathbf{r}'|=v_st$ (ref. ⁴⁶). According to equation (2), a detector placed at position \mathbf{r} will sense a propagating optoacoustic wave $p(\mathbf{r}, t)$ at time t , which was generated at any point

on the spherical surface $S'(t)$ at $t=0$ due to the illumination of the medium with a light pulse. For OPAM, the pressure signal $p(\mathbf{r}, t)$ (equation (2)) is measured at multiple positions \mathbf{r} , on or close to the boundary of the object being imaged. Image reconstruction then implies the use of equation (2) to compute the distribution of $p_0(\mathbf{r}')$ from $p(\mathbf{r}, t)$ measurements obtained at these multiple positions (further mathematical details of this inversion process are provided in section 1 of the Supplementary Information).

Geometrical configurations. Two major geometrical configurations are typically considered for mesoscopic optoacoustic imaging. The first OPAM configuration is geared toward epi-illumination measurements of tissue, and detects ultrasound signals at locations along a line or a two-dimensional grid. Typically, a single detector is scanned to capture optoacoustic signals along the line or grid (Fig. 1a–d), giving rise to raster-scan OPAM (RSOM)^{47–51}. RSOM employs broad-beam illumination (Fig. 1a), and its image formation and resolution are governed by ultrasonic diffraction and detector specifications. Image formation typically requires mathematical inversion (Fig. 1e,f)^{48,52–54}. Multi-element arrays can also be employed as alternatives to single-element detectors^{55–58}. However, OPAM based on single detectors generally offers superior imaging performance compared to multi-element arrays, since higher quality detection characteristics can be achieved with single detectors. For comparison, we note that both OPAM and AR optoacoustic microscopy rely on raster-scan schemes and broad illumination, yet the latter is geared towards resolving finer structures. However, to reach microscopic resolutions, AR optoacoustic microscopy requires higher central frequencies than OPAM (Table 1). Yet because the attenuation of sound by tissue increases with frequency, the use of higher frequencies limits the penetration depth of AR optoacoustic microscopy (with respect to OPAM)^{30,31,59}. Conversely, optical or OR optoacoustic microscopy scans focus light beams (Fig. 1g,h), and the resolutions that they achieve depend on the optical focus^{60–63}. Moreover, although image deconvolution or the mathematical processing of images may be used to improve image fidelity or resolution^{64–66}, the formation of OR microscopy images does not necessarily require mathematical inversion^{1,59,67}.

The second OPAM configuration detects optoacoustic signals over a curved (typically, cylindrical or spherical) surface (Fig. 1i). Reported implementations involve single-element transducers⁶⁸ or

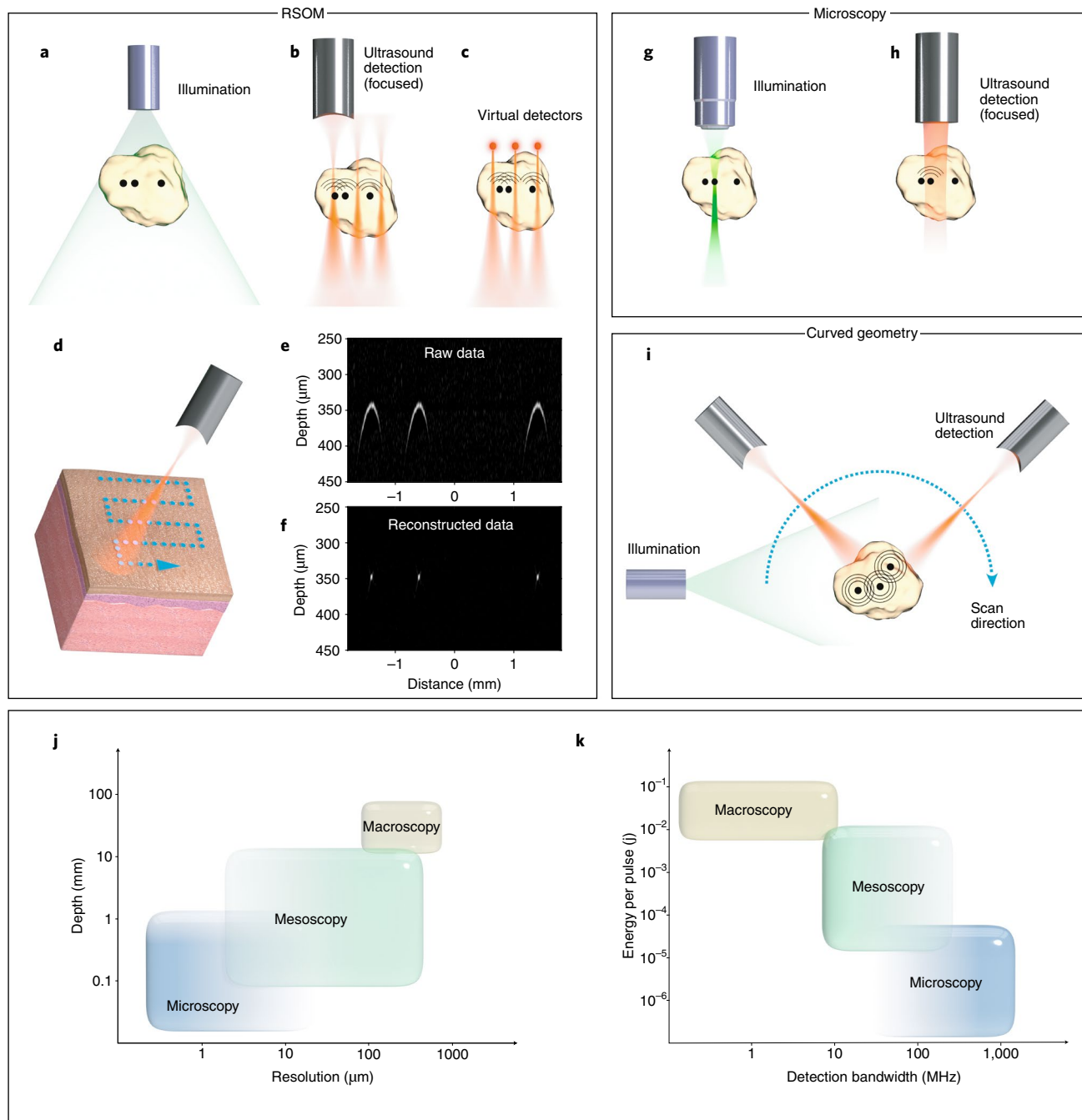


Fig. 1 | Scanning implementations and operational regimes of OPAM. **a–d**, Raster scan OPAM (RSOM). **a**, A wide-field illuminating light beam excites ultrasound waves in the sample. Black dots represent point absorbers. **b**, The generated ultrasound signals are detected within confined volumes generated by the focal points of spherically focused transducers. **c**, The detection process is approximated by using point detectors (termed virtual detectors), which are assumed to be located at the acoustic focus. **d**, Raster-scan pattern, shown on a simplified schematic representing the skin. **e**, Raw data generated from three point absorbers, as schematized in panels **a–c**. **f**, The mathematical inversion of the raw data in panel **e** generates an accurate tomographic representation of the point objects. **g,h**, Optoacoustic microscopy uses focused illumination (**g**), whereas RSOM uses broad-beam illumination (**h**). **i**, Curved-geometry OPAM. All scanning implementations can be realized with detector arrays instead of single-element transducers; however, single-element transducers lead to better image quality. **j,k**, Operational characteristics of OPAM, compared to optoacoustic microscopy and macroscopy, for depth and resolution (**j**), and for energy and detection bandwidth (**k**).

multi-element ultrasound-transducer arrays rotated around the sample⁶⁹. Performing OPAM with detection over curved surfaces that enclose the sample leads to better resolution isotropy and image quality than RSOM, because a larger part of the ultrasound wave-front propagating away from the imaged object can be captured. Therefore, datasets collected over curved surfaces typically contain

more information than raster scans, and lead to images of enhanced content and quality. Conversely, raster-scan approaches are better suited for a range of clinical applications that only allow one-sided scans, for example when using handheld scanners.

Besides the geometrical configuration, the imaging performance of OPAM also depends on detector specifications and illumination

energy that generally differ from the settings used in macroscopy or microscopy (Table 1 and Fig. 1j,k).

Optoacoustic detection. Detector specifications play a critical role on the image quality of OPAM. An ultrasound detector is characterized by the detector's geometry, including the active area employed for sound detection (detection cross-section), the ability to focus sound waves, the central frequency of operation, the detection bandwidth and the sensing principle of operation. Moreover, the selection of single-element or multiple-element detector arrays affects the detection specifications. The most common detector technology employed is piezoelectric sound detection, which is also used in ultrasound imaging^{70,71}, but optical sensing of sound is increasingly considered for high-quality image performance^{53,72,73}.

Bandwidth, depth and resolution. The image resolution and imaging depth crucially depend on the bandwidth of the ultrasound wave that is captured⁴⁷. In general, higher ultrasound frequencies lead to better image resolution, albeit at more superficial depths, owing to the depth-dependent attenuation of high-frequency ultrasound in tissue^{70,74,75} (Supplementary Fig. 1, Supplementary Sections 2 and 5). Therefore, frequency selection enables the transition from microscopy to mesoscopy and macroscopy (Fig. 1k). The bandwidth of the generated pressure wave (equation (2)) depends on the duration of the illuminating pulse and the geometrical properties of the absorbers in the medium imaged, with narrower pulses exciting broader signals (Fig. 2a). The typical bandwidths that are generated in tissues illuminated by ultrafast (<2 ns) pulses reach up to 250–300 MHz, which correspond to resolutions below 10 µm.

Mesoscopy generally operates in the few tens of MHz, allowing imaging at depths of several millimetres (Table 1). This frequency band can be captured by common piezoelectric detectors (Fig. 2b), leading to resolutions in the 30–100 µm range. Nevertheless, such detectors do not generally capture the entire bandwidth of optoacoustic waves generated in tissues by laser pulses of a few nanoseconds. Lithium niobate (LiNbO_3)-based single-element detectors have enabled imaging at bandwidths larger than 150 MHz (refs. ^{32,47,48,54}), demonstrating performance gains over narrower bandwidth selection⁴⁸ (Fig. 2c). This UWB performance leads to mesoscopic systems that reach several millimetres in depth, yet also retains microscopic resolution at more superficial depths. For example, in phantom measurements, RSOM at bandwidths larger than 100 MHz, using <2 ns excitation-pulse widths, exhibited an axial resolution of less than 10 µm at depths of 2–3 mm (refs. ^{47,48}). However, UWB acquisition comes with new requirements for data processing and image reconstruction. In particular, the separation of low and high frequencies improves the reconstruction quality and representation of the high-frequency components in the UWB-RSOM image^{32,48} (Fig. 2d and Supplementary Section 4).

Alternatively, Fabry-Pérot interferometric detectors, also implemented in RSOM geometries, have led to mesoscopic performance with large fields of view at central frequencies and at bandwidths of ~40 MHz (ref. ⁵⁰), achieving 55–65 µm in resolution and ~10 mm in depth^{49,50,76}. Recently, fibre Bragg gratings (FBGs) have achieved detection bandwidths of ~100 MHz (ref. ⁷⁷) while maintaining high sensitivity, similarly to piezoelectric transducers with larger detection areas⁷⁸. FBG technology is, therefore, also relevant for mesoscopic applications. In particular, the small form factors of FBG-based detectors may allow their integration into intravascular or endoscopic optoacoustic systems.

Mesoscopy can also be carried out with multi-element ultrasound arrays⁷⁹. However, it is challenging to manufacture ultrasound element arrays of high sensitivity with central frequencies and bandwidths beyond 20–30 MHz (refs. ^{56,80}). Capacitive micro-machined ultrasound transducers may offer an alternative capable of providing up to double the bandwidth of piezoelectric detector

arrays⁸¹. Nevertheless, current manufacturing challenges to achieve UWB performance, such as the dicing of small ultrasound elements or the proper amplification of weak and high-frequency signals collected from small ultrasound elements, may limit the use of arrays in high-resolution mesoscopic implementations (Fig. 3a,k).

Detection cross-section, sensitivity and resolution. The detection cross-section—that is, the active area of detection of ultrasound waves—also affects the quality of optoacoustic images. Generally, the smaller the cross-sectional area the better the lateral resolution; however, a physically smaller detection cross-section also leads to lower detection sensitivity^{75,82}. A preferred solution that addresses this trade-off is what is known as 'virtual detector' (Fig. 1c), a concept that is based on spherically focused detectors. In this case, the cross-sectional area at the focal point of the detector is assumed to be the active-detection cross-section. Assuming transducers of piezoelectric technology, this implementation offers virtual detectors of very small effective collection area but higher sensitivity compared to the use of an ultrasound element, with actual dimensions equal to the focus area of the focused element (for example, a 20-µm radius)^{41,47}. Conversely, spherical focusing is not generally applicable to the detection elements of ultrasound arrays. Therefore, many high-quality mesoscopy systems are still implemented with a single scanning detector. Conversely, the use of arrays in mesoscopic applications may limit imaging performance due to limitations not only in the detection frequency and bandwidth but also the minimum active detection area that can be achieved by the elements in the array (Fig. 3a,k).

The use of optical interferometry^{50,72,78,83,84} or optical-beam deflection^{85,86} can serve as an alternative to the virtual-detector principle. Since optical resonators and optical beams can have cross-sections of extremely small physical dimensions, optical detection can provide sound detectors with active areas in the micrometre range (or smaller), offering an advantage over focused piezoelectric elements.

Generally, the bandwidth plays a critical role in defining the axial OPAM resolution, whereas the cross-section size primarily affects the lateral resolution, especially in RSOM geometries (Supplementary Information Section 2). In curved geometries, both parameters play a central role in defining the resolution of the OPAM system (Supplementary Information Section 3). In all cases, the bandwidth, cross-section and overall detector characteristics must be matched to the depth and resolution specifications of the desired application.

Acceptance angle. The acceptance angle of the detector employed also plays a critical role in image formation. In analogy to optical lenses with a high numerical aperture, optoacoustic-signal collection over a broader acceptance angle improves the resolution and overall image quality (Fig. 2e). For example, during RSOM imaging of a KPL4 breast tumour xenograft in a mouse, acceptance angles of 15 degrees only allow for visualization of vessels parallel to the detector (Fig. 2f). However, increasing the acceptance angle reveals vessels tilted at larger angles with respect to the detector, offering a more accurate representation of the sample imaged (Fig. 2f). Geometries that use curved-detection arrangements (Fig. 1i) dynamically adapt the acceptance angle (synthetic aperture) by rotating and translating the detector around the sample^{55,87}, effectively improving image quality with respect to systems that only allow for translational displacements of the detector.

Tomographic image formation. Similarly to optical macroscopy, image reconstruction on the basis of forward modelling and mathematical inversion of optoacoustic recordings collected over multiple angles (projections) is a necessary step in mesoscopy, because the signals collected are generated within a large, diffusively illuminated volume over time and cannot otherwise form a high-resolution

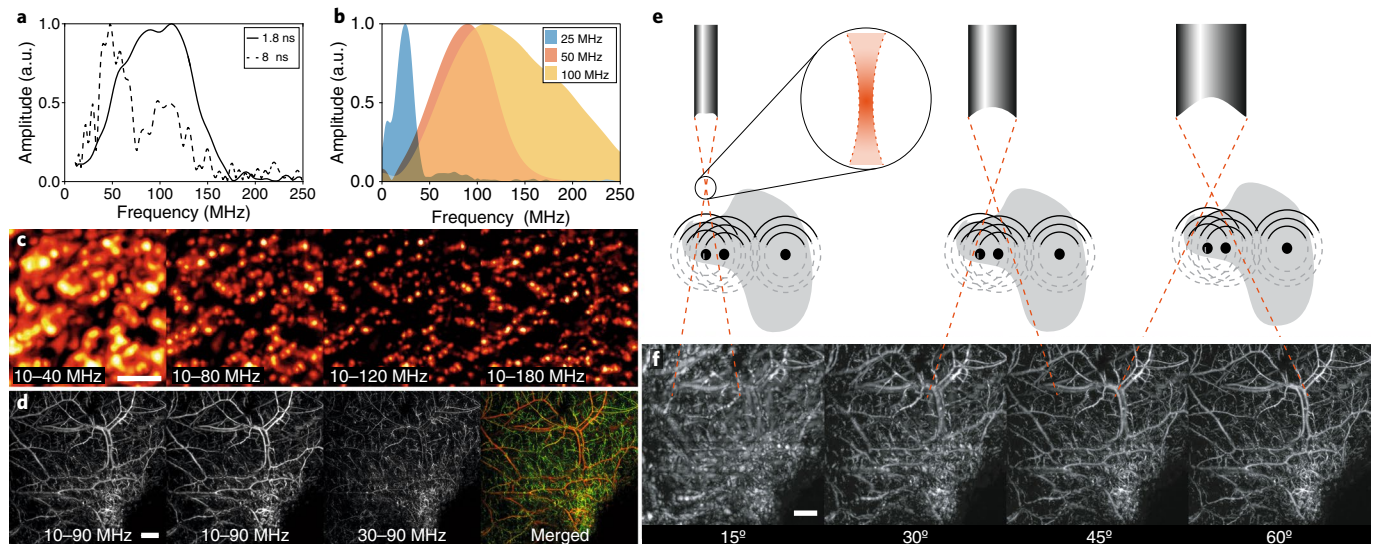


Fig. 2 | Effects of detector bandwidth, aperture and angle of acceptance, on the performance of optoacoustic imaging. **a**, Experimental data of the optoacoustic bandwidth generated by illuminating a 10 µm microsphere with 1.8-ns and 8-ns laser pulses. The use of shorter pulses generates a much broader range of frequencies from the same sample. **b**, Comparison of bandwidth responses of detectors with nominal central frequencies of 25 MHz, 50 MHz and 100 MHz (these bandwidths correspond to actual detectors measured at the Institute for Biological and Medical Imaging & the Chair for Biological Imaging HMGU/TUM in Munich, Germany). **c**, Experimental images of the human-skin capillary loops reconstructed by using increasing bandwidths of 30 MHz, 70 MHz, 110 MHz and 170 MHz, exhibiting improvements in resolution and image quality with increasing bandwidth. **d**, Images obtained from a KPL4 breast-tumour xenograft in a mouse *in vivo*, using reconstructions based on all frequencies (10–90 MHz), a low-frequency sub-band (10–30 MHz), a high-frequency sub-band (30–90 MHz), and the combination of low-frequency and high-frequency sub-bands following equalization (merged; green, small vessels; red, large vessels). Separate reconstruction and visualization of low and high frequencies enables better representation of the high-frequency details, which may not be clearly visible otherwise (that is, when comparing the 10–90 MHz to the 10–30 MHz image). **e**, Depending on aperture and focusing characteristics, a detector can collect signals over different angles of acceptance. Inset, magnified focal region. **f**, Experimental results of increasing angle of acceptance for imaging a KPL4 breast-tumour xenograft in a mouse. As the acceptance angle increases from 15° to 60°, the vasculature and other image features are better resolved. Scale bars, 500 µm (**c**); 2 mm (**d,f**). Panel **a** reproduced from ref. ⁴⁷. The Optical Society; panel **b**. Credit: Dominik Soliman; panel **c** reproduced from ref. ³², Springer Nature Ltd.

image^{40,88–93}. The forward and inversion methods employed can also affect image quality. Three key aspects of tomographic image reconstruction (Supplementary Information Section 1) enable imaging features that are not generally found in optical or OR optoacoustic microscopy. First, by using mathematical inversion, a two-dimensional scan suffices for the acquisition of the information needed for a three-dimensional reconstruction. Second, reconstruction approaches enable the use of data collected from entire volumes, which leads to higher signal-to-noise ratios (SNRs) in comparison to methods that seek to optimize resolution by rejecting signals outside a narrow focal point or line (the use of virtual detectors, Fig. 1c, and of detection elements with large-acceptance angles and apertures, is particularly beneficial for achieving a high SNR)⁸². Third, reconstruction approaches can account for the parameters of the experimental set-up, such as the exact angular coverage or the spatial sensitivity characteristics of a transducer (Fig. 2c). In particular, model-based inversion methods can describe the characteristics of the experimental setup and of sound propagation in tissue, and are well-suited to account for various experimental parameters (Supplementary Information Section 1)^{94–105}.

Illumination and spectral unmixing. Several operational parameters of optoacoustic imaging, such as the penetration depth or the acquisition speed, depend on the energy per pulse and on the repetition rate of the light source. Therefore, the selection of an appropriate illuminator technology also plays a key role in OPAM performance. Repetition rates of typical pulsed-laser sources employed in mesoscopic systems are in the 1–10 kHz range, which leads to scan times in the range of a few seconds to minutes, depending

on the desired field of view (FOV) of the image. Faster imaging can be achieved with faster lasers or by using detector arrays, the latter leading to video-rate implementations²³. Common mesoscopy implementations illuminate tissue with light pulses of energies in the range of a few hundred microjoules to a few millijoules per pulse^{32,75}. For biological measurements, the energies and scanning speeds are restricted by the maximum permitted exposure limits (defined by the American National Standards Institute).

A commonly available wavelength for optoacoustic imaging is 532 nm, generated as a second harmonic of the Nd:YAG (neodymium-doped yttrium aluminium garnet) crystal. However, a particularly beneficial feature of the optoacoustic method is the ability to illuminate at multiple wavelengths and subsequently use unmixing techniques to resolve the concentration of different photoabsorbers in each voxel of the image^{106,107}. Although most implementations so far use a small number of wavelengths (typically two), an increased number of wavelengths offers improvements in sensitivity and quantification^{106,108}. Tuneable sources based on dye lasers or optical parametric oscillators can be employed for illumination at multiple wavelengths¹⁰⁹, but typically offer slow tuning rates of several seconds per wavelength. For this reason, recent advances in multispectral optoacoustics are geared toward light sources that achieve fast wavelength tuning (which are especially relevant for eventual clinical applications)²³.

Spectral unmixing in optoacoustic imaging (reviewed in ref. ¹⁰⁷) remains a particularly active research topic. The optoacoustic spectral problem presents a unique challenge, as it is three-dimensional in nature and is affected by optical-fluence attenuation as a function of depth and wavelength (spectral colouring). Although this effect

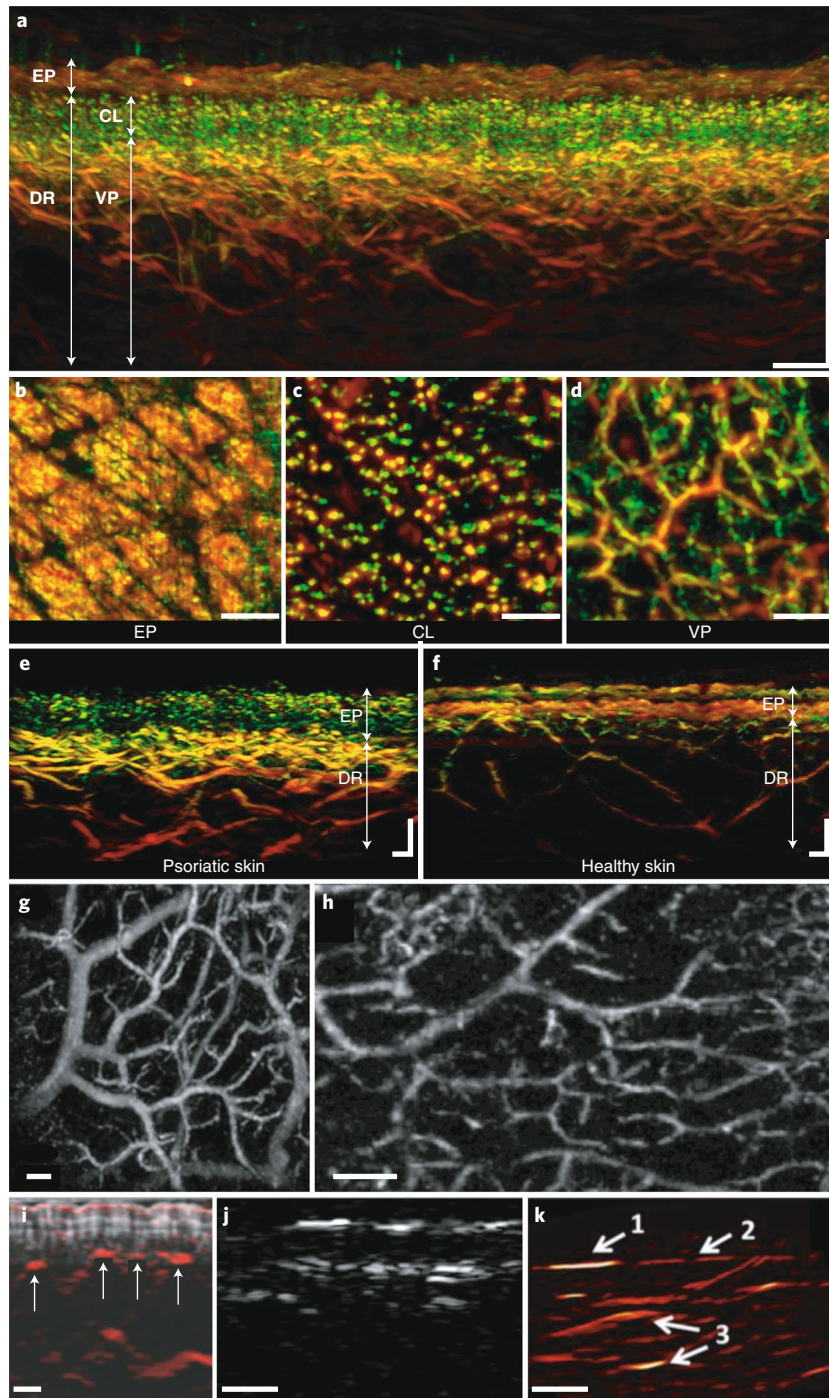


Fig. 3 | Skin imaging using OPAM. **a–f**, RSOM of healthy and psoriatic skin at 180 MHz in bandwidth. **a**, Representative image of healthy skin. EP, epidermis; DR, dermis; CL, capillary loops; VP, vascular plexus. **b–d**, Maximum-intensity projections of the skin layers in panel **a**; epidermis (**b**), capillary loops (**c**) and vascular plexus (**d**). **e,f**, Comparison of psoriatic skin (**e**) and healthy skin (**f**) imaged at 50 MHz. **g**, Morphological OPAM imaging of the skin vasculature, shown from the top, imaged using a 39-MHz optical detector. **h**, Maximum-intensity projection of the vasculature in the human palm, using RSOM at 35 MHz. **i**, Hybrid RSOM-OCT (red and grey scale, respectively) image of human skin. RSOM was acquired using an optical detector with a -3 decibel bandwidth of 39 MHz; arrows point to vessels in the vascular plexus. **j**, Coronal images of the skin, acquired with RSOM using a 35-MHz single-element PZT (lead-zirconate-titanate) detector. **k**, OPAM of the human skin using a 24-MHz linear array multi-element transducer; arrow (1) points to a mole, arrow (2) points to the skin surface, and arrows (3) point to the upper and lower boundaries of a vessel. In **i–k** the lower bandwidth precludes the image performance and resolution seen in panel **a** (180 MHz in bandwidth). Scale bars, 500 µm (**a–d,i,j**), 200 µm (**e–f**), 1 mm (**g,h,k**). Panels **a–f** reproduced from ref.³², Springer Nature Ltd; panels **g,i** reproduced from ref.⁵³, The Optical Society; panels **h,j** reproduced from ref.¹³⁰, IEEE; and panel **k** reproduced from ref.⁵⁶, IEEE.

does not strongly affect superficial measurements, new methods (such as EigenSpectra unmixing¹⁰⁶) that employ data analysis in the spectral domain can account for spectral colouring deeper in tissue.

Illumination in the frequency domain. An alternative to illumination based on light pulses (time domain) is illumination via continuous-wave (CW) light of modulated intensity (frequency domain),

in which case the amplitude and phase of the ultrasound waves are detected at the corresponding modulation frequency. In this case, accurate image formation requires that light be modulated at multiple frequencies; for example, over the same bandwidth as the one generated by ultrafast pulses^{98,110}. Although still in development, frequency-domain illumination may ultimately allow simultaneous illumination at multiple wavelengths carried at different frequencies, with pulse-compression techniques enhancing the SNR (ref. ¹¹¹), and chirp pulses sweeping through multiple frequencies^{111,112}.

Mesoscopy applications

A new range of applications can be uniquely assessed by OPAM. In the following, we discuss the types of imaging contrast available to optoacoustic imaging, and the particular capabilities of OPAM for biological and medical imaging (Table 2).

Optoacoustic contrast. Optoacoustic methods resolve optical absorption of chromophores at given regions of the electromagnetic spectrum. For example, in the visible and near-infrared (NIR) spectral range (450–900 nm), haemoglobin and melanin have optical-absorption coefficients that are orders of magnitude greater than those of other intrinsic light absorbers, such as collagen, lipids or water^{23,26,29}. As a result, OPAM can measure vascular parameters, tissue oxygenation or melanin distribution with high contrast without the need for exogenous labels^{32,51}. Moreover, because water and lipids absorb radiation strongly in the 900–1,700 nm wavelength range, it is also possible to image them using appropriate wavelength selection^{113,114}. Nevertheless, many label-free OPAM implementations operate in the visible region of the spectrum, where haemoglobin and melanin show the highest optical absorption. Detailed images of microvasculature (concentrated haemoglobin) and melanin distribution can be resolved at a single wavelength. To separate the contributions of different light absorbers (such as oxygenated haemoglobin, deoxygenated haemoglobin and melanin), the sample can be illuminated at multiple wavelengths, giving rise to maps of optical-absorption spectra, which are then analysed via spectral-unmixing techniques¹⁰⁹. This intrinsic contrast can be employed for resolving and quantifying various pathologies, including tissue hypoxia and inflammation^{115,116}.

Contrast agents have been also employed for imaging a wider range of biological and pathophysiological parameters^{39,117}. Commonly used contrast agents are fluorescent dyes and nanoparticles (in particular, gold nanoparticles and fluorochrome-encapsulating liposomes)^{44,118–123}. Nanoparticles carrying loads of organic fluorochromes yield absorption cross-sections that are comparable to metal nanoparticles, and may show better photostability and lower toxicity than their metal counterparts^{118,119,124}. Targeted optical quenchers have also been considered¹²⁵.

The use of contrast agents enables the imaging of cell permeability, protease and receptor upregulation, inflammation, and several other physiological and biological processes^{24,39}. Melanin is an excellent endogenous optoacoustic contrast agent, and can be expressed exogenously in desired cells by insertion of the tyrosinase gene (analogous to the targeted expression of fluorescent proteins in optical microscopy^{50,126,127}). An even wider range of biological processes *in vivo* may become accessible to optoacoustic imaging through the development of reporters, such as photoswitchable labels^{128,129}, that offer detection with higher SNR (refs. ^{128,129}). Although the use of exogenous contrast agents may prove invaluable for both discovery-driven and translational research, efforts to implement OPAM in clinical settings are currently only focused on imaging with endogenous contrast.

Dermatology. Several optoacoustic implementations have been considered for skin imaging. However, most implementations employed narrow bandwidths that are inappropriate for high-fidelity

cross-sectional imaging⁵⁹. Portable UWB RSOM has recently been considered for the quantification of psoriasis-associated skin inflammation without the need for exogenous contrast agents³². Skin illumination performed at 532 nm enabled the detailed visualization of skin layers and vascular morphology (Fig. 3a–d), reaching axial resolutions of up to 4.5 μm, and lateral resolutions of 18.4 μm in the first skin layers (Fig. 3a)³² and tens of micrometres at deeper layers. Different psoriasis and inflammation biomarkers could be quantified in three dimensions, such as elevated epidermal thickness (acanthosis), capillary-loop elongation, capillary-loop dilation, dermal vasculature vasodilation and increased microvascular volume (Fig. 3e,f). The quantification of these features led to the derivation of an RSOM-based objective severity index, which correlated with the psoriasis area severity index (PASI), the current gold standard. However, whereas PASI is determined on the basis of a subjective and qualitative assessment of the skin surface, the objective severity index is based on a quantitative multifactorial assessment of skin features, such as vessel rarefaction, total blood volume, epidermal thickness and fractal number³². This development promises to bring dermatology observations closer to the demands of precision medicine. UWB RSOM was also shown to be capable of quantifying inflammation biomarkers in eczema, vasculitis and nevus-associated vasculature³². The potential of UWB RSOM can be extended by exciting the sample with multiple wavelengths. Images recorded at 20 wavelengths in the 450–650 nm region¹⁰⁹ revealed eumelanin in epidermal tissue, as well as vascularization and oxygen saturation in deeper dermal layers. Blood-oxygenation measurements ranged from 50% to 84%, in accordance with estimates based on diffuse optical imaging¹⁰⁹.

OPAM in the few tens of MHz (that is, at 30–100 μm in resolution) has also been considered for dermatology, but it revealed only a limited subset of morphological and physiological features when compared to UWB RSOM. Raster-scan implementations at <40 MHz could visualize subcutaneous vessels with diameters larger than 50 μm^{53,130–132}, but not the microvasculature resolved by UWB RSOM (Fig. 3g–j). Likewise, mesoscopy based on a multi-element 24-MHz linear array could only detect general boundaries of the skin or large vessels, but not a detailed view of the vasculature or of capillary loops⁷⁹ (Fig. 3k). Imaging at 20 MHz enabled visualization of the degradation of surgical sutures, and the localization of externally administered stem cells labelled with gold nanorods in wounds of a rat model of burn injury^{97,133,134}. Optoacoustic imaging at even lower frequencies (10 MHz; ~200 μm in resolution) was applied by using a linear ultrasound array to assess, in laboratory rats, the depth of burns^{135,136}; in addition to allowing for clear demarcation of injury depth, which exhibited good correlation with histological findings, the linear ultrasound array revealed neovascularization below the injured tissue. OPAM of melanomas has also been considered but has so far been limited to the imaging of animal models^{137,138}.

OPAM opens a way to assessing and quantifying chronic inflammation, angiogenesis, injury and healing in a label-free mode, and it may allow the visualization of tissue response to drugs, cosmetics and environmental factors, such as temperature and chemicals. The method could be useful for studying how systemic diseases manifest in the skin, such as during the progression of diabetes, cardiovascular diseases and metabolic diseases. Unlike OCT (refs. ^{139–141}) or high-frequency skin ultrasound^{142–144}, which primarily reveal tissue interfaces and tissue morphology, OPAM visualizes specific molecules (such as haemoglobin and melanin) and can resolve functional contrast over a larger FOV than optical microscopy, thus complementing existing skin-imaging methods, such as OCT, high-frequency ultrasound imaging and reflectance confocal imaging.

Intravascular optoacoustic imaging. OPAM has also demonstrated potential for extending the capabilities of intravascular

Table 2 | Example applications of OPAM

Area	Disease	Features imaged	Dimensions of feature offered	References
Dermatology	Cancer Psoriasis Eczema Burn Cosmetics	Inflammation Acanthosis Melanin-layer thickness Lesion borders and depth Rarefaction Total blood volume Vasculature morphology Angiogenesis Vasodilation Oxygenation and hypoxia Hair and hair follicles	Depth imaged, 1–4 mm in burn depth or in the dermis Area scanned, >0.25–1 cm ²	32,53,54,130,137,138,211
Intravascular imaging	Plaque characterization Assessment of vessel-wall condition	Lipids Haematoma Vascularization Plaque morphology Inflammation	Depth imaged, 5–7 mm in plaque depth Area scanned, 360 degrees × 5–10 cm in length	113,114,148–154,207,212–215
Endoscopy	Cancer staging Barret's oesophagus Colitis / Crohn's disease	Wall and tumour morphology Vascular morphology Angiogenesis Oxygenation and hypoxia Total blood volume	Depth imaged, 3–4 mm Area scanned, 360 degrees × 5–10 cm in length	156,157,159,160,216
Small-animal imaging	Neuroimaging Cancer Vascular disease Organ visualization	Oxygenation and hypoxia Perfusion Vascular morphology Tissue morphology Neuronal activity (with labels) External labels	Depth imaged, 7–8 mm Volume scanned, <1 cm ³	49,51,52,57–59,76,80,83,87, 125,132,167,175,185,217–220
Developmental biology	Phenotyping adult organisms Functional imaging	Deep-seated fluorescent proteins or optoacoustic reporters Tissue morphology Vascularization Oxygenation and hypoxia	Depth imaged, 4–5 mm, whole-body Volume scanned, <25 mm ³	47,49,68,73,87,186,189,221

ultrasound (IVUS) in interventional cardiology. IVUS is performed by rotating and translating (pull back) a miniaturized ultrasound detector within a catheter system inserted into the lumen of blood vessels^{145–147}. The detector transmits and records ultrasound waves, forming three-dimensional ultrasound images of the vessel wall. These images are used to characterize the presence and burden of atherosomatous plaques in arteries, and potentially to assess the placement or condition of a stent. Optoacoustic images can be formed by adding an optical light guide (optical fibre) to the ultrasound system and by using the ultrasound detector both for detecting ultrasound and optoacoustic signals. The resulting hybrid ultrasound-optoacoustic catheter (Fig. 4a) combines morphology information based on ultrasound contrast, with complementary optoacoustic measurements of morphology, molecular content and pathophysiology.

Hybrid IVUS-optoacoustic implementations have resolved, for example, lipid-rich regions in excised aortas of New Zealand rabbits fed with a mild cholesterol diet^{148–150}. With multi-wavelength illumination of atherosclerotic human coronary arteries at wavelengths around 1,200 nm, the hybrid method yielded spectra matching those of cholesterol oleate and cholesterol linoleate¹⁵¹, and coronary lipids have also been imaged *in vivo* at 1,700 nm in a swine model of coronary arterial disease (Fig. 4b)¹¹⁴ and in atherosclerotic arteries in a rabbit model^{152,153}. One disadvantage of OPAM at these wavelengths is the need to clear the water (and blood) from the vessel lumen, because water strongly attenuates optical excitation at >1,000 nm¹¹⁴. Clearance is achieved by administering a bolus of deuterated-water saline during imaging^{114,154} (this is analogous to the clearance procedure of blood for intravascular OCT)¹⁴⁷. Since

data must be acquired along long vessel segments during flushing, scan times of a few seconds or less are needed. However the speed of OPAM implementations is restricted by the repetition rate (typically in the kHz range) of the laser. Therefore, a major current challenge of prototype hybrid IVUS-optoacoustic implementations is the need to accelerate repetition rates or to use frequency-domain illumination and reduce scan times (an important prerequisite for clinical applications).

Endoscopy. OPAM features developed and tested in dermatology can be translated to the endoscopic imaging of the gastrointestinal tract and other tissue lumens and cavities. Two types of miniaturized scanning systems have been considered: a raster-scan geometry (Fig. 1d) in a small, forward-looking scope¹⁵⁵, and geometries and scanning approaches based on design elements from intravascular-imaging systems. The forward-looking design may limit the FOV of mesoscopy, and may be better suited for optical or optoacoustic-microscopy implementations, possibly combined with white-light endoscopy. In the approaches inspired by intravascular imaging, a single detector is rotated around its own axis to radially scan hollow organs such as the oesophagus or the colon, and at the same time it is pulled back through the lumen in order to generate images of the entire organ. Variations on this principle have been proposed, including the rotation of both the detector and the optical illuminators (Fig. 4c–e)¹⁵⁶, the rotation of the illuminator only and detection based on a stationary omnidirectional detector⁷⁸, and the rotation of a parabolic mirror to direct both optical and acoustic energy to and from tissue (Fig. 4f–h)^{157–159}.

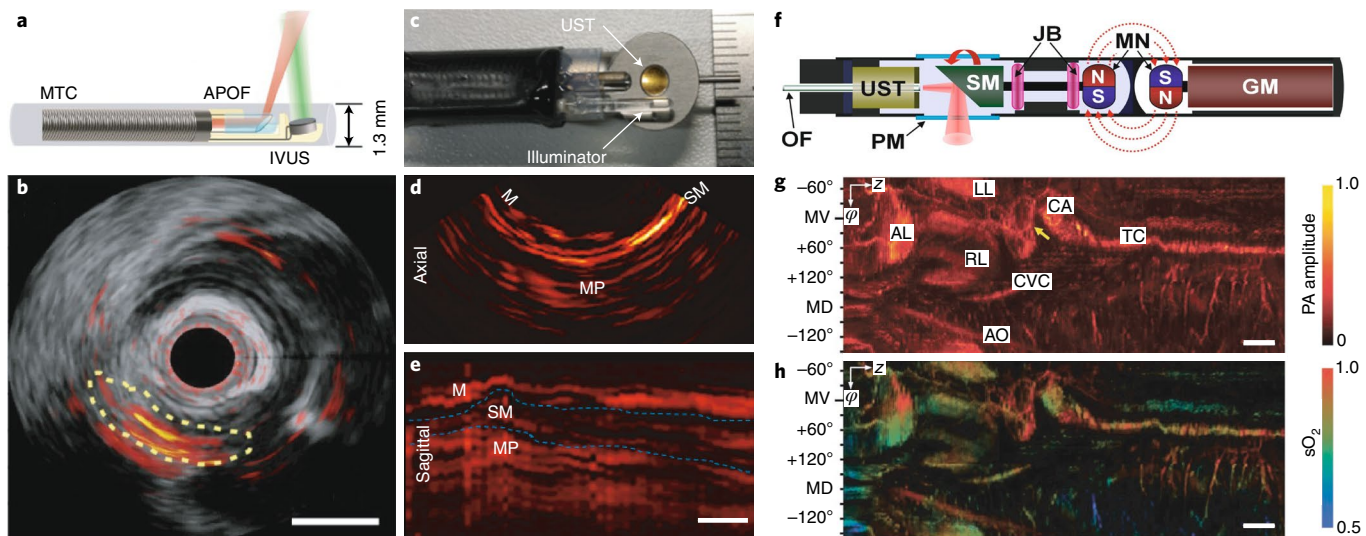


Fig. 4 | Optoacoustic endoscopy. **a**, Schematic of an optoacoustic intravascular catheter. An intravascular ultrasound (IVUS) transducer (detector) is combined with a miniaturized optoacoustic endoscope inside a polyethylene sheath. The optical signal (red) and the acoustic signal (green) are rotated using a parabolic mirror. APOF, angle-polished optical fibre; MTC, metal torque coil. **b**, Representative hybrid optoacoustic–ultrasound image of coronary arterial disease in a swine, obtained at a wavelength of 1,700 nm. The yellow dashed lines demarcate a stent visualized on the basis of lipid contrast. **c–e**, Optoacoustic endoscopy based on rotating both the ultrasound transducer (UST) and the illumination source. **c**, Photograph of the distal end of the catheter. **d,e**, Axial (**d**) and sagittal (**e**) images of a swine oesophagus, obtained with the system in **c**. M, mucosa; SM, submucosa; MP, muscularis propria; the dashed lines in **e** represent the boundaries of the different oesophagus layers. **f**, Optoacoustic endoscopy based on a parabolic rotating mirror with a static ultrasound transducer and illumination source. The mirror rotates both the acoustic field and the optical-illumination beam. GM, geared micromotor; JB, jewel bearings; MN, magnets; OF, optical fibre; PM, plastic membrane; SM, scanning mirror. **g**, Radial maximum-intensity optoacoustic projection spanning 360° of a rabbit oesophagus, showing total haemoglobin concentration, obtained using the system in panel **f** at 584 nm. AL, accessory lobe; LL, left lobe; RL, right lobe of the lung; AO, aorta; CVC, caudal vena cava; CA, carina; TC, trachea; MV, mid ventral position; MD, mid-dorsal position. **h**, Functional radial maximum-intensity projection showing oxygen saturation (sO_2) for the image from panel **g** by using data collected at 562 nm and 584 nm. Scale bars, 1 mm (**b,e**), 1 cm (**g,h**). Panels **a,b** reproduced from ref.¹¹⁴, The Optical Society; panels **c–e**. Credit: Andreas Buehler; panel **f** reproduced from ref.¹⁵⁹, The Optical Society; and panels **g,h** reproduced from ref.¹⁵⁷, Springer Nature Ltd.

Optoacoustic endoscopy has been employed to image the vascularization of the oesophagus in adult New Zealand rabbits *in vivo*¹⁵⁸ (at 584 nm; 36 MHz; 55 μ m axially and 80 μ m laterally) and the lymphatic system surrounding the gastrointestinal tract (at 640 nm) after contrast enhancement with Evans-blue dye¹⁵⁷. Replacing line-scan geometries with curved-scanning improves on problems of limited view angle, and enhances image quality¹⁶⁰. The combination of optical and acoustic focus at 20 MHz allows hybrid microscopy and mesoscopy imaging¹⁵⁶. Further miniaturization can be achieved by using micro-ring resonators¹⁶¹; for example, a ring-array endoscope was employed for the *ex vivo* imaging of a swine oesophagus, yet at a reduced resolution (320 μ m; 6 MHz)¹⁶².

OPAM endoscopy could be employed for staging disease, evaluating the extent of tumour borders and detecting the presence of early-stage disease that manifests as sub-surface pathophysiological alterations^{163,164} (Table 2). In analogy to optoacoustic dermoscopy, optoacoustic endoscopy may contribute to quantifying cancer- and inflammation-related biomarkers, such as total blood volume, vessel dilation, vascular rarefaction during surveillance studies, and tissue oxygenation and viability during surgical procedures^{23,26,157}. OPAM endoscopy could be implemented on its own or in combination with other modalities, such as OCT (ref. ¹⁶⁵).

Translational imaging. By extending the penetration depth of optical microscopy, mesoscopy can provide new abilities in studying tissues. In particular, mesoscopy visualizes volumes that are at least two orders of magnitude larger than the volumes accessible by optical microscopy, and thus in principle it can detect the spatial heterogeneity of optical contrast, which would be difficult with other methods.

Cancer. Two major motivations for applying OPAM to cancer have been the label-free imaging of angiogenesis and hypoxia (Fig. 5a, b), which are not possible by any other imaging method, and the visualization of much larger volumes than those imaged by microscopy. Raster-scan implementations of OPAM have enabled label-free imaging of angiogenesis in melanoma mouse models^{137,166} and the monitoring of drug-induced vascular disruption in human colorectal adenocarcinoma xenografts^{76,166,167}. In contrast to optical microscopy, RSOM visualized microvasculature deeper in tissue and over a larger FOV without the need to remove the skin or to implant optical windows^{51,168}, yielding a non-invasive alternative to optical methods, albeit at lower resolutions than optical microscopy. Cancer OPAM using linear arrays is also possible¹³⁸ (680 nm; 21 MHz). Moreover, the use of multiple wavelengths allows for measurements of tissue oxygenation and consequently of hypoxia^{109,169}, which has diagnostic and theranostic implications. Similarly, RSOM imaging using two wavelengths (584 nm and 764 nm; 50 MHz) distinguished between the darker tumour cells (B16 melanoma cells) and the vasculature⁵⁹.

In addition to intrinsic tissue absorption, mesoscopic imaging of cancer can benefit from the use of exogenous contrast (in analogy to multispectral optoacoustic tomography^{23,26,44}). For example, tyrosinase-expressing K562 leukaemia cells and 293T human embryonic kidney cells were imaged in high detail at depths of 10 mm (RSOM at 22 MHz and 600 nm; Fig. 5c,d)⁵⁰. Likewise, labelled optical quenchers were employed to visualize in high detail the expression of $\alpha_v\beta_3$ -integrin in U87 spheroids and in subcutaneously implanted U87 tumours¹²⁵. Curved geometry OPAM may be better suited for a more detailed visualization of cancer (Fig. 1i), by resolving

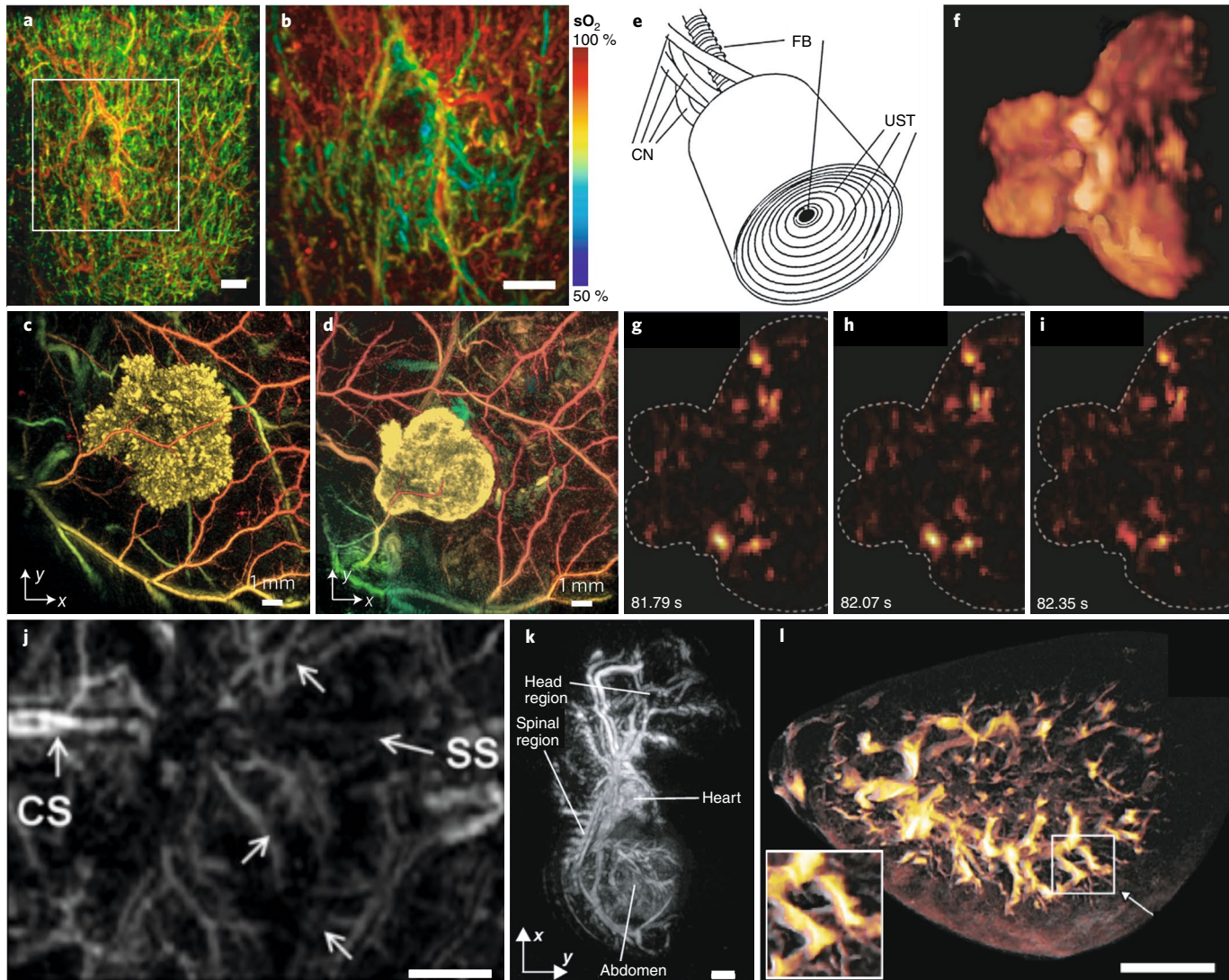


Fig. 5 | Translational imaging with OPAM. **a**, Maximum-intensity projection RSOM image of a KPL4 breast-cancer xenograft in mice at 532 nm, showing detailed vasculature (red, 10–30 MHz; green, 30–90 MHz). **b**, Oxygen saturation ($s\text{O}_2$) image of the white-box region in panel **a**. The $s\text{O}_2$ image was produced by imaging at four wavelengths (520, 540, 560 and 590 nm) followed by linear unmixing. **c,d**, RSOM images of tyrosinase-expressing K562 cells (central yellow mass) embedded subcutaneously in the mouse flank. Images were taken at day 0 (right after cell implantation) in panel **c** and at day 15 in panel **d**. **e**, Spherical detector array for volumetric optoacoustic imaging. UST, ultrasound transducer (consisting of 256 elements); FB, fibre bundle; CN, connecting cables. **f**, Real-time volumetric mesoscopic optoacoustic imaging of a zebrafish brain in resting state at 10 MHz using the detector shown in panel **e**. **g–i**, Activation patterns evoked in response to pentylenetetrazole neurostimulation at the time points shown. **j**, Non-invasive optoacoustic imaging of the cortex vasculature in a mouse brain, arrows indicate feeding/draining vessels in the mouse's somatosensory cortex; SS, sagittal sinus; CS, coronal suture. **k**, Maximum-intensity projection images, using interferometric RSOM at 22 MHz, of the thorax and abdominal cavity of a mouse on embryonic day 15.5 ex vivo. **l**, Imaging of murine kidneys ex vivo using curved geometry OPAM. The mouse had been injected with gold nanorods 15 minutes prior to euthanasia. Spectrally unmixed images of gold nanorods overlaid in yellow over a single-wavelength optoacoustic image at 765 nm. Inset, magnification of the region pointed to by an arrow. Scale bars, 1 mm. Panels **c,d** reproduced from ref.⁵⁰, Springer Nature Ltd.; panel **e** reproduced from ref.²¹⁰, Elsevier; panels **f–i** reproduced from ref.¹⁷⁰, Springer Nature Ltd.; panel **j** reproduced from ref.¹⁷², SPIE; panel **k** reproduced from ref.⁴⁹, SPIE; and panel **l** reproduced from ref.⁸⁰, The Optical Society.

features through the entire mass of solid tumours at a more isotropic resolution than RSOM (ref. ¹⁶⁷). The imaging of enhanced-permeability-and-retention effects has also been shown with curved-geometry implementations, by imaging the distribution of exogenously administered gold nanoparticles¹⁶⁷.

Neuroimaging. OPAM is also becoming popular in neuroimaging investigations in animal models, primarily due to the unique combination of contrast, penetration, resolution and fast scan-times. Real-time volumetric OPAM was recently developed for brain imaging,

based on a hemispherical curved-geometry transducer array of 256 or 512 detector elements (Fig. 5e). Frequencies at the interface between mesoscopy and macroscopy (~10 MHz) enabled real-time ex vivo monitoring of calcium dynamics and neurovascular coupling in living zebrafish brains expressing the calcium indicator GCaMP5G (Fig. 5f–i)¹⁷⁰. However, imaging the mouse brain structure and perfusion has only been possible so far with macroscopic implementations¹⁷¹.

The cortical vasculature of mice has also been imaged *in vivo* through the intact scalp, at depths of ~1–2 mm, by using RSOM

at 20 MHz (refs. ^{172,173}) or 50 MHz (refs. ^{174,175}), involving dye-laser illumination at 561 nm and 570 nm, respectively. Major vascular landmarks, including the sagittal sinus, middle cerebral artery and coronal suture, were recorded at lateral and axial resolutions of, respectively, 70 μm and 54 μm (Fig. 5j). Although visible wavelengths only allowed the imaging of superficial cortex signals⁵², deeper imaging was achieved at longer wavelengths. Vascular landmarks deeper in the brain, including the sinus rectus and the inferior sagittal sinus, the latter seen extending to a depth of 3.1 mm⁵², were visible at wavelengths larger than 630 nm. At even longer wavelengths (889 nm) the inferior sagittal sinus was seen extending down to a greater depth (~3.7 mm)⁵². Nevertheless, in addition to imaging vascular landmarks, another key attraction for brain OPAM is the imaging of haemodynamic responses, recorded as changes in the concentrations of oxygenated and deoxygenated haemoglobin over time^{170,172,176–181}.

Other applications. Several studies have demonstrated the potential of OPAM for other biomedical applications, such as the imaging of cardiovascular dynamics in a mouse heart *in vivo* by using a linear array operating at 30 MHz (ref. ⁵⁷), and video-rate scans of the heart (532 nm) and of heart oxygenation (559 nm) at 50 MHz (ref. ⁵⁸). RSOM at 22 MHz can be used for analysing organ development by imaging the cardiovascular system of mouse embryos both inside the mother and *ex vivo* (Fig. 5k)⁴⁹. Inflammation responses associated with rheumatoid arthritis have also been visualized¹¹⁵. RSOM at 50 MHz of endothelial cells incubated with gold nanorods conjugated to intercellular adhesion molecule-1 showed that, after treatment, the rods bound selectively to cells with the pro-inflammatory cytokine interferon-gamma^{182,183}.

Curved-geometry mesoscopy^{55,80} at 24 MHz has been used to image the highly detailed distribution of gold nanoparticles within murine kidneys⁸⁰ *ex vivo* (Fig. 5l) without the need for organ clearing. However, in this study the distribution of the IRDye 800CW was only possible at 6 MHz because of the larger volume occupied by the fluorochrome (compared with the gold nanoparticles). Multispectral curved-geometry studies at 15 MHz have visualized fluorescent proteins labelling the imaginary disks of *Drosophila melanogaster* and adult zebrafish *in vivo* at resolutions of ~35 μm ⁶⁸. Higher-quality images of *D. melanogaster* and juvenile zebrafish (Fig. 6a) at 7–15 μm in resolution were achieved at depths of 2–3 mm by using RSOM and curved-geometry implementations at 50–100 MHz (refs. ^{47,87}).

Microscopy and mesoscopy

Microscopy and mesoscopy have different operational characteristics. Nonetheless, they can be combined in a single system that complements the imaging depths and the contrast-generating mechanisms of each approach. In the following, we compare microscopy and mesoscopy, and describe hybrid systems of them.

OPAM versus microscopy. AR optoacoustic imaging exchanges depth for resolution, and aims at high-resolution interrogations through several millimetres of tissue. AR optoacoustic microscopy requires high frequencies and bandwidths that may reach the Gigahertz range³¹. However, the increasing attenuation of ultrasound signals at increasing frequency forces high-resolution AR optoacoustic microscopy to image only at depths from a few tens of micrometres to hundreds of micrometres. At lower frequencies, reduction in ultrasound attenuation allows for a gradual shift from AR optoacoustic microscopy to AR optoacoustic mesoscopy, the latter reaching depths of several millimetres but at resolutions that range in the several tens of micrometres (Fig. 1j). Moreover, compared to microscopy approaches, larger FOVs and volumes are imaged in the mesoscopic regime (at similar scan times). For this reason, light-source specifications also change between microscopy

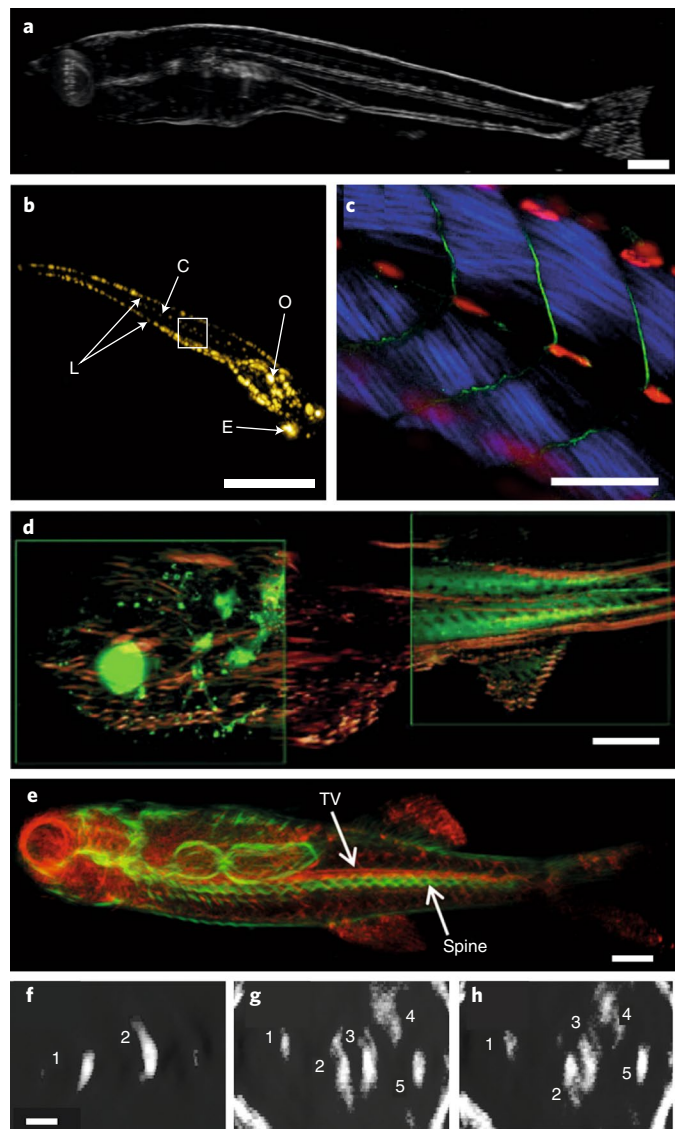


Fig. 6 | OPAM in development applications. **a**, Maximum-intensity projection obtained using curved-geometry mesoscopy, showing the side view of a juvenile zebrafish (21 days old). **b**, Maximum-intensity projection of an RSOM image of a larva zebrafish (6 days old), showing the central melanocyte stripe (C), eyes (E), lateral melanocyte stripe (L), and inner organs (O). **c**, Zoom-in of the region marked by a white box in **b** using hybrid optoacoustic-multiphoton microscopy. The optoacoustic-microscopy signal (red) marks the melanocytes. The second-harmonic generation signal (blue) shows different muscle structures (myomeres) constituting the musculature of the fish body. The third-harmonic-generation signal (green) reveals the regions between the myomeres most probably representing myosepta, which are thin sheets of connective tissue separating and supporting the myomeres. **d**, Hybrid imaging combining OPAM (brown) and single-sheet illumination microscopy (SPIM, green) of an adult zebrafish (2 months old), showing that the resolution of OPAM is higher than that of SPIM when imaging adult fish, due to the increased photon scattering over few-days-old fish. **e**, Hybrid OPAM-ultrasound microscopy of a juvenile zebrafish. Red, OPAM; green, ultrasound microscopy; TV, tail vein. **f–h**, Different cross sections through a *D. melanogaster* pupa, imaged at 50 MHz and 532 nm. Numbers 1–5 correspond to different DsRed-expressing cells in the central nervous system of the *D. melanogaster* pupae. Scale bars, 1 mm (**a,b,e**), 100 μm (**c,f**). Panel **a** reproduced with permission from ref. ⁸⁷, Springer Nature Ltd.; panels **b,c** reproduced from ref. ¹⁸⁷, Springer Nature Ltd.; panel **d** reproduced from ref. ¹⁸⁶, Wiley; panel **e** reproduced from ref. ¹⁸⁹, SPIE; and panels **f–h** reproduced from ref. ¹⁹¹, AIP.

and mesoscopy, with the latter generally delivering up to several orders of magnitude higher energy in tissue, for deeper visualization (Fig. 1k). Therefore OPAM enables biological imaging *in vivo* at regimes largely inaccessible to optical microscopy and optoacoustic microscopy (Table 1 and Fig. 1j,k).

In contrast to the scalability seen within AR optoacoustic microscopy and mesoscopy, OR optoacoustic microscopy involves FOVs and penetration depths that are similar to optical microscopy²⁹. Therefore, the application span of OR optoacoustic microscopy may be limited, considering the rich contrast and high sensitivity already achieved by optical-microscopy techniques developed for a broad range of tissue-imaging and cellular-imaging applications. Nevertheless, a distinct difference between optical and optoacoustic microscopy is label-free imaging. Label-free optoacoustic microscopy visualizes microvasculature and more generally tissue absorption, whereas label-free optical microscopy may resolve cellular morphology (on the basis of auto-fluorescence) or collagen structures¹⁸⁴ (via tissue-anisotropy contrast).

Hybrid optical and optoacoustic imaging. The combination of OPAM and optical microscopy, or OR optoacoustic microscopy, extends optical interrogation to deeper tissues^{175,185–187}, offering visualization across scales that are not accessible by any of the techniques on their own. By using broadband-frequency detection, optoacoustic systems can reach resolutions spanning a few micrometres within the first 1–1.5 mm of depth to tens of micrometres several millimetres deep²⁹, thus spanning the whole mesoscopy range. Moreover, recent hybrid implementations capitalize on the extended scale offered by combining OPAM and optical, and/or OR optoacoustic, microscopy (Fig. 6a). In particular, RSOM has been combined with OR optoacoustic and multiphoton microscopy for the multiscale imaging of zebrafish (Fig. 6b,c) and mouse tissue^{187,188}. In another implementation, mesoscopy at 24 MHz was combined with selective-plane illumination microscopy (SPIM) for the multiscale imaging of model organisms common in developmental biology (Fig. 6d)^{67,186}. The hybrid system enabled the imaging of transgenic zebrafish, and showed that for larger fish (2 months old) the optoacoustic method provides higher resolution than SPIM, since the latter is affected by photon scattering^{67,186}.

Hybrid-imaging modalities not only merge scales but can also combine the contrast offered by the two modalities. For example, systems combining optoacoustics and ultrasound^{189,190} can visualize the internal organs of zebrafish (Fig. 6e)¹⁸⁹. A multimodal system combining fluorescence, autofluorescence, second-harmonic and third-harmonic generation, and spectral absorption optoacoustics, showcased the benefits of having extended readings of diverse contrast in a single device¹⁸⁴. Moreover, the imaging of DsRed (using RSOM at 50 MHz and at 15/61 μm axial/lateral resolutions; Fig. 6f–h) or of mCherry (with curved-geometry OPAM) in labelled *D. melanogaster* pupae^{68,191} and zebrafish⁶⁸, points to the additional possibility of highly detailed fluorescence protein microscopy corroborated by hybrid OPAM imaging at larger scales (yet lesser resolution). Furthermore, mesoscopy images obtained over a large FOV can be used to guide microscopy examinations to specific points of interest on the mesoscopy image¹⁸⁷.

Outlook

Optoacoustic macroscopy is emerging as a clinical modality for detecting cancer^{34,192–201} (such as metastatic melanoma^{202,203}) and for disease staging (as shown in Crohn's disease^{37,204,205}) but operates with characteristics that generate a performance gap when compared to the resolution and FOV captured by optical or optoacoustic microscopy (Fig. 1j,k; Table 1). With its unique combination of high resolution and the capacity to image through several millimetres of tissue, OPAM bridges microscopic and macroscopic imaging techniques. Unlike optical microscopy or optoacoustic

macroscopy, penetration depth in the mesoscopic regime is primarily limited by the attenuation of high-ultrasound frequencies, rather than by light attenuation, in tissue⁷⁴. The frequency bandwidth detected plays a central role in the resolution achieved as a function of depth. UWB OPAM at ~200 MHz bandwidth can image morphological and pathophysiological features over depths of a few millimetres, compared to implementations at narrower bandwidths (Fig. 4). Nevertheless, the resolution achieved is not uniform with depth. Since higher ultrasound frequencies undergo higher attenuation, OPAM generally detects a narrower bandwidth compared to the requirements of AR optoacoustic microscopy. Likewise, UWB OPAM essentially offers hybrid microscopy–mesoscopy performance. Importantly, by enabling imaging at volumes that could be two orders of magnitude larger than those typical of microscopy methods, OPAM's performance cannot be matched by using purely optical-imaging methods.

OPAM exploits contrast that is fundamentally different from other high-resolution imaging modalities such as HFUS or OCT, which primarily resolve tissue morphology on the basis of the reflection of sound or light from tissue interfaces. In contrast, optoacoustic imaging visualizes optical absorption from tissue molecules or nanoparticles, which means that it offers morphological, functional and molecular contrast that may complement HFUS or OCT. With spectral unmixing, multispectral OPAM can sense and differentiate multiple molecules and particles along the spectral dimension²³, revealing functional and molecular characteristics of the tissue that HFUS and OCT cannot sense. Moreover, OPAM may allow imaging through several millimetres of tissue (depending on the frequency employed), unlike the fundamentally limited depth (due to photon scatter) offered by OCT.

An important development in OPAM relates to the imaging of biomarkers of pathophysiology and disease. For example, single-wavelength UWB OPAM can provide quantitative measurements of inflammatory biomarkers (such as vessel dilation, tortuosity and total blood volume) without the need for exogenous labels³²; such metrics may facilitate precision-medicine implementations in dermatology and endoscopy, for a more rigorous and objective monitoring of disease progression and treatment efficacy²⁰⁶. The addition of multi-wavelength illumination and spectral unmixing can extend label-free imaging capabilities to the imaging of oxygenation and hypoxia¹⁰⁹, fat, lipids, water content^{150,151,207}, and melanin¹⁰⁹. OPAM can thus monitor, in a label-free mode, an array of biomolecules and features relevant to health and disease.

The imaging features of OPAM could be clinically useful in the assessment of systemic skin conditions^{32,130,137}, in oncology^{32,75,137}, in cardiovascular medicine, and for studies of metabolic disorders such as diabetes. For example, many diseases involving inflammation and alterations in metabolism, such as cancer, psoriasis, tissue remodelling and diabetes, involve perturbations in angiogenesis and tissue oxygenation²⁰⁸. Moreover, the development of hybrid OPAM systems could further extend imaging capabilities by combining the advantages of microscopy and mesoscopy, and by enabling multi-scale label-free imaging of tissue pathophysiology. Further development of contrast agents and targeted probes for optoacoustic imaging may also expand the biological and clinical applications of OPAM. Hybrid OPAM systems already permit specific imaging of an extended range of biological targets and functions, such as receptor and enzyme expression^{23,39}. Dedicated contrast-enhancement strategies, such as reporter genes^{50,126,127} and photoswitchable proteins^{128,129,209}, are also applicable to optoacoustic imaging. Such developments can expand the range of molecules and processes that can be visualized by OPAM in the laboratory, and enable biological imaging at depths inaccessible to optical microscopy.

To achieve the full potential of OPAM, further advances in system hardware and computational algorithms are required. The detection sensitivity of optoacoustic imaging is fundamentally

limited by current detection technologies, which were originally designed to meet the needs of ultrasonography. In ultrasound imaging, the power of the ultrasound pulses emitted can generally be increased to compensate for weak detector sensitivity. However, this practice is not generally possible in optoacoustic imaging because of laser-safety limits defined by the American National Standards Institute. Therefore, detectors of increased sensitivity are required for OPAM. Also needed are better light sources that enable illumination at multiple wavelengths via nanosecond-range pulse widths. Tuneable lasers and high-energy pulsed-light sources that operate at multiple wavelengths remain expensive, and generally have low repetition rates (<10 kHz) and wavelength tuning speeds (>1 sec) that limit the implementation of multispectral RSOM. The laser-repetition rate limits the scanning speed of RSOM and the FOV that can be inspected in a certain time period. Conversely, although the use of multi-element ultrasound arrays could accelerate scan times, high-performance OPAM based on array technology is challenging to achieve because of difficulties in balancing high bandwidths, small detection areas and high-sensitivity by using array technology. Moreover, improvements in tomographic reconstruction and image analysis can also improve image quality and quantification, for example via techniques superior to simple filtered back-projection, including model-based approaches or methods that account for fluence effects, or for the electrical or total impulse response of the system^[31]. We expect that the emergence of clinical applications based on optoacoustic technology will drive advances in the design and fabrication of light detectors and light sources, thus improving the performance of mesoscopy.

Received: 5 June 2017; Accepted: 1 March 2019;

Published online: 15 April 2019

References

1. Helmchen, F. & Denk, W. Deep tissue two-photon microscopy. *Nat. Methods* **2**, 932–940 (2005).
2. Theer, P., Hasan, M. T. & Denk, W. Two-photon imaging to a depth of 1000 μm in living brains by use of a Ti: Al 2 O 3 regenerative amplifier. *Opt. Lett.* **28**, 1022–1024 (2003).
3. Smith, A. M., Mancini, M. C. & Nie, S. Second window for *in vivo* imaging. *Nat. Nanotechnol.* **4**, 710 (2009).
4. Hong, G. et al. Ultrafast fluorescence imaging *in vivo* with conjugated polymer fluorophores in the second near-infrared window. *Nat. Commun.* **5**, 4206 (2014).
5. Vakoc, B. J. et al. Three-dimensional microscopy of the tumor microenvironment *in vivo* using optical frequency domain imaging. *Nat. Med.* **15**, 1219–1223 (2009).
6. Drexler, W. et al. Ultrahigh-resolution ophthalmic optical coherence tomography. *Nat. Med.* **7**, 502 (2001).
7. Fujimoto, J. G. Optical coherence tomography for ultrahigh resolution *in vivo* imaging. *Nat. Biotechnol.* **21**, 1361 (2003).
8. Čížnář, T., Mazilu, M. & Dholakia, K. *In situ* waveform correction and its application to micromanipulation. *Nat. Photon.* **4**, 388–394 (2010).
9. Chaigne, T. et al. Controlling light in scattering media non-invasively using the photoacoustic transmission matrix. *Nat. Photon.* **8**, 58–64 (2014).
10. Vellekoop, I. M., Lagendijk, A. & Mosk, A. Exploiting disorder for perfect focusing. *Nat. Photon.* **4**, 320–322 (2010).
11. Katz, O., Small, E. & Silberberg, Y. Looking around corners and through thin turbid layers in real time with scattered incoherent light. *Nat. Photon.* **6**, 549–553 (2012).
12. Ertürk, A. et al. Three-dimensional imaging of solvent-cleared organs using 3DISCO. *Nat. Prot.* **7**, 1983 (2012).
13. Hama, H. et al. ScaleS: an optical clearing palette for biological imaging. *Nat. Neurosci.* **18**, 1518 (2015).
14. Dodt, H.-U. et al. Ultramicroscopy: three-dimensional visualization of neuronal networks in the whole mouse brain. *Nat. Methods* **4**, 331 (2007).
15. Farkas, D. L. Invention and commercialization in optical bioimaging. *Nat. Biotechnol.* **21**, 1269–1271 (2003).
16. Weissleder, R. & Pittet, M. J. Imaging in the era of molecular oncology. *Nature* **452**, 580–589 (2008).
17. Vinegoni, C., Pitsouli, C., Razansky, D., Perrimon, N. & Ntziachristos, V. *In vivo* imaging of *Drosophila melanogaster* pupae with mesoscopic fluorescence tomography. *Nat. Methods* **5**, 45 (2008).
18. Sharpe, J. et al. Optical projection tomography as a tool for 3D microscopy and gene expression studies. *Science* **296**, 541–545 (2002).
19. Ntziachristos, V., Ripoll, J., Wang, L. V. & Weissleder, R. Looking and listening to light: the evolution of whole-body photonic imaging. *Nat. Biotechnol.* **23**, 313–320 (2005).
20. Weissleder, R. A clearer vision for *in vivo* imaging. *Nat. Biotechnol.* **19**, 316–316 (2001).
21. Maugh, T. H. Photoacoustic spectroscopy: New uses for an old technique. *Science* **188**, 38–39 (1975).
22. Rosencwaig, A. & Gershoff, A. Theory of the photoacoustic effect with solids. *J. Appl. Physics* **47**, 64–69 (1976).
23. Taruttis, A. & Ntziachristos, V. Advances in real-time multispectral optoacoustic imaging and its applications. *Nat. Photon.* **9**, 219–227 (2015).
24. Taruttis, A., van Dam, G. M. & Ntziachristos, V. Mesoscopic and macroscopic optoacoustic imaging of cancer. *Cancer Res.* **75**, 1548–1559 (2015).
25. Wang, L. V. & Yao, J. A practical guide to photoacoustic tomography in the life sciences. *Nat. Methods* **13**, 627 (2016).
26. Wang, L. V. & Hu, S. Photoacoustic tomography: *in vivo* imaging from organelles to organs. *Science* **335**, 1458–1462 (2012).
27. Maslov, K., Zhang, H. F., Hu, S. & Wang, L. V. Optical-resolution photoacoustic microscopy for *in vivo* imaging of single capillaries. *Opt. Lett.* **33**, 929–931 (2008).
28. Yao, J., Maslov, K. I., Zhang, Y., Xia, Y. & Wang, L. V. Label-free oxygen-metabolic photoacoustic microscopy *in vivo*. *J. Biomed. Opt.* **16**, 076003 (2011).
29. Ntziachristos, V. Going deeper than microscopy: the optical imaging frontier in biology. *Nat. Methods* **7**, 603–614 (2010).
30. Strohm, E. M., Berndl, E. S. L. & Kolios, M. C. Probing Red Blood Cell Morphology Using High-Frequency Photoacoustics. *Biophys. J.* **105**, 59–67 (2013).
31. Strohm, E. M., Berndl, E. S. L. & Kolios, M. C. High frequency label-free photoacoustic microscopy of single cells. *Photoacoustics* **1**, 49–53 (2013).
32. Aguirre, J. S. et al. Precision assessment of label-free psoriasis biomarkers with ultra-broadband optoacoustic mesoscopy. *Nat. Biomed. Eng.* **1**, 0068 (2017).
33. Alentalo, T. et al. High-resolution three-dimensional imaging of islet-infiltrate interactions based on optical projection tomography assessments of the intact adult mouse pancreas. *J. Biomed. Opt.* **13**, 054070 (2008).
34. Piras, D., Xia, W., Steenbergen, W., van Leeuwen, T. G. & Manohar, S. Photoacoustic imaging of the breast using the twente photoacoustic mammoscope: present status and future perspectives. *IEEE J. Quantum Elect.* **16**, 730–739 (2010).
35. Diot, G. et al. Multispectral optoacoustic tomography (MSOT) of human breast cancer. *Clin. Cancer Res.* **23**, 6912–6922 (2017).
36. Oraevsky, A. et al. Full-view 3D imaging system for functional and anatomical screening of the breast. In *Proc. SPIE 10494* <https://doi.org/10.1117/12.2318802> (2018).
37. Knieling, F. et al. Multispectral Optoacoustic Tomography for Assessment of Crohn's Disease Activity. *New Engl. J. Med.* **376**, 1292–1294 (2017).
38. Reber, J. et al. Non-invasive measurement of brown fat metabolism based on optoacoustic imaging of hemoglobin gradients. *Cell Metab.* **27**, 689–701 (2018).
39. Weber, J., Beard, P. C. & Bohndiek, S. E. Contrast agents for molecular photoacoustic imaging. *Nat. Methods* **13**, 639–650 (2016).
40. Xu, M. & Wang, L. V. Photoacoustic imaging in biomedicine. *Rev. Sci. Instrum.* **77**, 041101 (2006).
41. Li, M.-L., Zhang, H. F., Maslov, K., Stoica, G. & Wang, L. V. Improved *in vivo* photoacoustic microscopy based on a virtual-detector concept. *Opt. Lett.* **31**, 474–476 (2006).
42. Westervelt, P. J. & Larson, R. S. Laser-excited broadside array. *J. Acoust. Soc. Am.* **54**, 121–122 (1973).
43. Diebold, G., Sun, T. & Khan, M. Photoacoustic monopole radiation in one, two, and three dimensions. *Phys. Rev. Lett.* **67**, 3384 (1991).
44. Ntziachristos, V. & Razansky, D. Molecular imaging by means of multispectral optoacoustic tomography (MSOT). *Chemical reviews* **110**, 2783–2794 (2010).
45. Xia, J., Yao, J. & Wang, L. V. Photoacoustic tomography: principles and advances. *Electromag. Waves* **147**, 1 (2014).
46. Deán-Ben, X. L. & Razansky, D. On the link between the speckle free nature of optoacoustics and visibility of structures in limited-view tomography. *Photoacoustics* **4**, 133–140 (2016).
47. Omar, M., Gateau, J. & Ntziachristos, V. Raster-scan optoacoustic mesoscopy in the 25–125 MHz range. *Opt. Lett.* **38**, 2472–2474 (2013).
48. Omar, M., Soliman, D., Gateau, J. & Ntziachristos, V. Ultrawideband reflection-mode optoacoustic mesoscopy. *Opt. Lett.* **39**, 3911–3914 (2014).
49. Laufer, J. et al. *In vivo* photoacoustic imaging of mouse embryos. *J. Biomed. Opt.* **17**, 061220 (2012).
50. Jathoul, A. P. et al. Deep *in vivo* photoacoustic imaging of mammalian tissues using a tyrosinase-based genetic reporter. *Nat. Photon.* (2015).

- Park, J. et al. Delay-multiply-and-sum-based synthetic aperture focusing in photoacoustic microscopy. *J. Biomed. Opt.* **21**, 036010 (2016).
- Laufer, J., Zhang, E., Raivich, G. & Beard, P. Three-dimensional noninvasive imaging of the vasculature in the mouse brain using a high resolution photoacoustic scanner. *Appl. Opt.* **48**, 299–306 (2009).
- Zhang, E. Z. et al. Multimodal photoacoustic and optical coherence tomography scanner using an all optical detection scheme for 3D morphological skin imaging. *Biomed. Opt. Exp.* **2**, 2202–2215 (2011).
- Aguirre, J. et al. Broadband mesoscopic optoacoustic tomography reveals skin layers. *Opt. Lett.* **39**, 6297–6300 (2014).
- Gateau, J., Chekkoury, A. & Ntziachristos, V. High-resolution optoacoustic mesoscopy with a 24 MHz multidetector translate-rotate scanner. *J. Biomed. Opt.* **18**, 106005 (2013).
- Vionnet, L. et al. 24-MHz scanner for optoacoustic imaging of skin and burn. *IEEE Trans. Med. Imag.* **33**, 535–545 (2014).
- Zemp, R., Song, L., Bitton, R., Shung, K. & Wang, L. Realtime photoacoustic microscopy of murine cardiovascular dynamics. *Opt. Exp.* **16**, 18551–18556 (2008).
- Wang, L., Maslov, K., Xing, W., Garcia-Uribe, A. & Wang, L. V. Video-rate functional photoacoustic microscopy at depths. *J. Biomed. Opt.* **17**, 106007 (2012).
- Zhang, H. F., Maslov, K., Stoica, G. & Wang, L. V. Functional photoacoustic microscopy for high-resolution and noninvasive *in vivo* imaging. *Nat. Biotechnol.* **24**, 848 (2006).
- Fiolka, R., Wicker, K., Heintzmann, R. & Stemmer, A. Simplified approach to diffraction tomography in optical microscopy. *Opt. Exp.* **17**, 12407–12417 (2009).
- Wicker, K., Mandula, O., Best, G., Fiolka, R. & Heintzmann, R. Phase optimisation for structured illumination microscopy. *Opt. Exp.* **21**, 2032–2049 (2013).
- Betzig, E. et al. Imaging intracellular fluorescent proteins at nanometer resolution. *Science* **313**, 1642–1645 (2006).
- Manley, S. et al. High-density mapping of single-molecule trajectories with photoactivated localization microscopy. *Nat. Methods* **5**, 155–157 (2008).
- Prevedel, R. et al. Simultaneous whole-animal 3D imaging of neuronal activity using light-field microscopy. *Nat. Methods* **11**, 727–730 (2014).
- Gustafsson, M. G. Surpassing the lateral resolution limit by a factor of two using structured illumination microscopy. *J. Microsc.* **198**, 82–87 (2000).
- Kim, T. et al. White-light diffraction tomography of unlabelled live cells. *Nat. Photon.* **8**, 256–263 (2014).
- Keller, P. J. Imaging morphogenesis: technological advances and biological insights. *Science* **340**, 1234168 (2013).
- Razansky, D. et al. Multispectral opto-acoustic tomography of deep-seated fluorescent proteins. *in vivo*. *Nat. Photon.* **3**, 412–417 (2009).
- Gateau, J., Caballero, M. Á. A., Dima, A. & Ntziachristos, V. Three-dimensional optoacoustic tomography using a conventional ultrasound linear detector array: Whole-body tomographic system for small animals. *Med. Phys.* **40** (2013).
- Szabo, T. L. *Diagnostic ultrasound imaging: inside out* (Acad. Press, 2004).
- Cobbold, R. S. *Foundations of biomedical ultrasound* (Oxford Univ. Press, 2006).
- Zhang, E. Z. & Beard, P. C. A miniature all-optical photoacoustic imaging probe. in *Proc. SPIE 7899* <https://doi.org/10.1117/12.874883> (2011).
- Nuster, R. et al. Hybrid photoacoustic and ultrasound section imaging with optical ultrasound detection. *J. Biophoton.* **6**, 549–559 (2013).
- Deán-Ben, X. L., Razansky, D. & Ntziachristos, V. The effects of acoustic attenuation in optoacoustic signals. *Phys. Med. Biol.* **56**, 6129 (2011).
- Schwarz, M. S. et al. Optoacoustic dermoscopy of the human skin: tuning excitation energy for optimal detection bandwidth with fast and deep imaging *in vivo*. *IEEE Trans. Med. Imaging* **36**, 1287–1296 (2017).
- Laufer, J. et al. *In vivo* preclinical photoacoustic imaging of tumor vasculature development and therapy. *J. Biomed. Opt.* **17**, 056016 (2012).
- Wissmeyer, G., Soliman, D., Shnaiderman, R., Rosenthal, A. & Ntziachristos, V. All-optical optoacoustic microscope based on wideband pulse interferometry. *Opt. Lett.* **41**, 1953–1956 (2016).
- Rosenthal, A. et al. Sensitive interferometric detection of ultrasound for minimally invasive clinical imaging applications. *Laser Photon. Rev.* **8**, 450–457 (2014).
- Schwarz, M., Buehler, A. & Ntziachristos, V. Isotropic high resolution optoacoustic imaging with linear detector arrays in bi-directional scanning. *J. Biophoton.* **8**, 60–70 (2015).
- Chekkoury, A. et al. Optical mesoscopy without the scatter: broadband multispectral optoacoustic mesoscopy. *Biomed. Opt. Exp.* **6**, 3134–3148 (2015).
- Rebling, J., Warshavski, O., Meynier, C. & Razansky, D. Optoacoustic characterization of broadband directivity patterns of capacitive micromachined ultrasonic transducers. *J. Biomed. Opt.* **22**, 041005 (2017).
- Oraevsky, A. A. & Karabutov, A. A. Ultimate sensitivity of time-resolved optoacoustic detection. in *Proc. SPIE 3916*, 228–239 (2000).
- Zhang, E., Laufer, J. & Beard, P. Backward-mode multiwavelength photoacoustic scanner using a planar Fabry-Perot polymer film ultrasound sensor for high-resolution three-dimensional imaging of biological tissues. *Appl. Opt.* **47**, 561–577 (2008).
- Beard, P. C., Hurrell, A. M. & Mills, T. N. Characterization of a polymer film optical fiber hydrophone for use in the range 1 to 20 MHz: A comparison with PVDF needle and membrane hydrophones. *IEEE T. Ultrason. Ferr.* **47**, 256–264 (2000).
- Maswadi, S. M. et al. All-optical optoacoustic microscopy based on probe beam deflection technique. *Photoacoustics* **4**, 91–101 (2016).
- Paltauf, G., Schmidt-Kloiber, H., Köstli, K. & Frenz, M. Optical method for two-dimensional ultrasonic detection. *Appl. Phys. Lett.* **75**, 1048–1050 (1999).
- Omar, M. et al. Optical imaging of post-embryonic zebrafish using multi orientation raster scan optoacoustic mesoscopy. *Light Sci. Appl.* **6**, e16186 (2017).
- Xu, M. & Wang, L. V. Universal back-projection algorithm for photoacoustic computed tomography. *Phys. Rev. E* **71**, 016706 (2005).
- Kostli, K. et al. Optoacoustic imaging using a three-dimensional reconstruction algorithm. *IEEE J. Sel. Top. Quant.* **7**, 918–923 (2001).
- Karaman, M., Li, P.-C. & O'Donnell, M. Synthetic aperture imaging for small scale systems. *IEEE T. Ultrason. Ferr.* **42**, 429–442 (1995).
- Köstli, K. P. & Beard, P. C. Two-dimensional photoacoustic imaging by use of Fourier-transform image reconstruction and a detector with an anisotropic response. *Appl. Opt.* **42**, 1899–1908 (2003).
- Oraevsky, A. A., Andreev, V. G., Karabutov, A. A. & Esenliev, R. O. Two-dimensional optoacoustic tomography: transducer array and image reconstruction algorithm. in *Proc. SPIE 3601 Laser Tissue Interaction X*. <https://doi.org/10.1117/12.350007> (1999).
- Kruger, R. A., Liu, P., Fang, Y. & Appledorn, C. R. Photoacoustic ultrasound (PAUS)—reconstruction tomography. *Med. Phys.* **22**, 1605–1609 (1995).
- Rosenthal, A., Razansky, D. & Ntziachristos, V. Fast semi-analytical model-based acoustic inversion for quantitative optoacoustic tomography. *IEEE T. Med. Imag.* **29**, 1275–1285 (2010).
- Caballero, M. Á. A., Rosenthal, A., Gateau, J., Razansky, D. & Ntziachristos, V. Model-based optoacoustic imaging using focused detector scanning. *Opt. Lett.* **37**, 4080–4082 (2012).
- Dean-Ben, X. L., Buehler, A., Ntziachristos, V. & Razansky, D. Accurate model-based reconstruction algorithm for three-dimensional optoacoustic tomography. *IEEE T. Med. Imag.* **31**, 1922–1928 (2012).
- Aguirre, J. et al. A low memory cost model based reconstruction algorithm exploiting translational symmetry for photoacoustic microscopy. *Biomed. Opt. Exp.* **4**, 2813–2827 (2013).
- Mohajerani, P., Tzoumas, S., Rosenthal, A. & Ntziachristos, V. Optical and optoacoustic model-based tomography: Theory and current challenges for deep tissue imaging of optical contrast. *IEEE Signal Proc. Mag.* **32**, 88–100 (2015).
- Anastasio, M. A., Zhang, J., Modgil, D. & La Rivière, P. J. Application of inverse source concepts to photoacoustic tomography. *Inverse Problems* **23**, S21 (2007).
- Huang, C., Wang, K., Nie, L., Wang, L. V. & Anastasio, M. A. Full-wave iterative image reconstruction in photoacoustic tomography with acoustically inhomogeneous media. *IEEE T. Med. Imag.* **32**, 1097–1110 (2013).
- Anastasio, M. A. et al. Half-time image reconstruction in thermoacoustic tomography. *IEEE T. Med. Imag.* **24**, 199–210 (2005).
- La Rivière, P. J., Zhang, J. & Anastasio, M. A. Image reconstruction in optoacoustic tomography for dispersive acoustic media. *Opt. Lett.* **31**, 781–783 (2006).
- Wang, K. & Anastasio, M. A. in *Handbook of Mathematical Methods in Imaging* 781–815 (Springer, New York, 2011).
- Wang, K., Su, R., Oraevsky, A. A. & Anastasio, M. A. Investigation of iterative image reconstruction in three-dimensional optoacoustic tomography. *Phys. Med. Biol.* **57**, 5399 (2012).
- Cox, B. T., Arridge, S. R., Köstli, K. P. & Beard, P. C. Two-dimensional quantitative photoacoustic image reconstruction of absorption distributions in scattering media by use of a simple iterative method. *Appl. Opt.* **45**, 1866–1875 (2006).
- Tzoumas, S. et al. Eigenspectra optoacoustic tomography achieves quantitative blood oxygenation imaging deep in tissues. *Nat. Commun.* **7**, 12121 (2016).
- Cox, B., Laufer, J. G., Arridge, S. R. & Beard, P. C. Quantitative spectroscopic photoacoustic imaging: a review. *J. Biomed. Opt.* **17**, 061202 (2012).
- Tzoumas, S., Deliolanis, N., Morscher, S. & Ntziachristos, V. Unmixing molecular agents from absorbing tissue in multispectral optoacoustic tomography. *IEEE T. Med. Imag.* **33**, 48–60 (2014).
- Schwarz, M., Buehler, A., Aguirre, J. & Ntziachristos, V. Three-dimensional multispectral optoacoustic mesoscopy reveals melanin and blood oxygenation in human skin. *in vivo*. *J. Biophoton.* **9**, 55–60 (2016).

110. Mohajerani, P., Kellnberger, S. & Ntziachristos, V. Frequency domain optoacoustic tomography using amplitude and phase. *Photoacoustics* **2**, 111–118 (2014).
111. Kellnberger, S., Deliolanis, N. C., Queirós, D., Sergiadis, G. & Ntziachristos, V. *In vivo* frequency domain optoacoustic tomography. *Opt. Lett.* **37**, 3423–3425 (2012).
112. Telenkov, S., Mandelis, A., Lashkari, B. & Forcht, M. Frequency-domain photothermoacoustics: Alternative imaging modality of biological tissues. *J. Appl. Phys.* **105**, 102029 (2009).
113. VanderLaan, D., Karpouli, A., Yeager, D. & Emelianov, S. Real-time intravascular ultrasound and photoacoustic imaging. *IEEE T. Ultrason. Ferr.* **64**, 141–149 (2016).
114. Wu, M. et al. Real-time volumetric lipid imaging *in vivo* by intravascular photoacoustics at 20 frames per second. *Biomed. Optics Exp.* **8**, 943–953 (2017).
115. Beziere, N. et al. Optoacoustic imaging and staging of inflammation in a murine model of arthritis. *Arthritis Rheumatol.* **66**, 2071–2078 (2014).
116. Mallidi, S., Luke, G. P. & Emelianov, S. Photoacoustic imaging in cancer detection, diagnosis, and treatment guidance. *Trends Biotechnol.* **29**, 213–221 (2011).
117. Liu, Y., Nie, L. & Chen, X. Photoacoustic molecular imaging: from multiscale biomedical applications towards early-stage theranostics. *Trends Biotechnol.* **34**, 420–433 (2016).
118. Beziere, N. et al. Dynamic imaging of PEGylated indocyanine green (ICG) liposomes within the tumor microenvironment using multi-spectral optoacoustic tomography (MSOT). *Biomaterials* **37**, 415–424 (2015).
119. Lozano, N., Al-Ahmady, Z. S., Beziere, N. S., Ntziachristos, V. & Kostarelos, K. Monoclonal antibody-targeted PEGylated liposome-ICG encapsulating doxorubicin as a potential theranostic agent. *Int. J. Pharm.* **482**, 2–10 (2015).
120. Wilson, K., Homan, K. & Emelianov, S. Biomedical photoacoustics beyond thermal expansion using triggered nanodroplet vaporization for contrast-enhanced imaging. *Nat. Commun.* **3**, 618 (2012).
121. Luke, G. P., Yeager, D. & Emelianov, S. Y. Biomedical applications of photoacoustic imaging with exogenous contrast agents. *Ann. Biomed. Eng.* **40**, 422–437 (2012).
122. Copland, J. A. et al. Bioconjugated gold nanoparticles as a molecular based contrast agent: implications for imaging of deep tumors using optoacoustic tomography. *Mol. Imag. Biol.* **6**, 341–349 (2004).
123. Conjeau, A. et al. Metallic nanoparticles as optoacoustic contrast agents for medical imaging. In *Proc. SPIE 6086 Photons Plus Ultrasound: Imaging and Sensing* <https://doi.org/10.1117/12.658065> (2006).
124. Gindy, M. E. & Prud'homme, R. K. Multifunctional nanoparticles for imaging, delivery and targeting in cancer therapy. *Expert Opin. Drug Del.* **6**, 865–878 (2009).
125. Haedicke, K. et al. Sonophore labeled RGD: a targeted contrast agent for optoacoustic imaging. *Photoacoustics* **6**, 1–8 (2017).
126. Stritzker, J. et al. Vaccinia virus-mediated melanin production allows MR and optoacoustic deep tissue imaging and laser-induced thermotherapy of cancer. *Proc. Natl Acad. Sci. USA* **110**, 3316–3320 (2013).
127. Paproski, R. J., Forbrich, A. E., Wachowicz, K., Hitt, M. M. & Zemp, R. J. Tyrosinase as a dual reporter gene for both photoacoustic and magnetic resonance imaging. *Biomed. Opt. Exp.* **2**, 771–780 (2011).
128. Stiel, A. C. et al. High-contrast imaging of reversibly switchable fluorescent proteins via temporally unmixed multispectral optoacoustic tomography. *Opt. Lett.* **40**, 367–370 (2015).
129. Yao, J. et al. Multiscale photoacoustic tomography using reversibly switchable bacterial phytochrome as a near-infrared photochromic probe. *Nat. Methods* **13**, 67–73 (2016).
130. Bost, W., Lemor, R. & Fournelle, M. Optoacoustic Imaging of subcutaneous microvasculature with a class one laser. *IEEE T. Med. Imag.* **33**, 1900–1904 (2014).
131. Kirillin, M., Perekatova, V., Turchin, I. & Subochev, P. Fluence compensation in raster-scan optoacoustic angiography. *Photoacoustics* **8**, 59–67 (2017).
132. Zhang, E., Laufer, J., Pedley, R. & Beard, P. *In vivo* high-resolution 3D photoacoustic imaging of superficial vascular anatomy. *Phys. Med. Biol.* **54**, 1035 (2009).
133. Aguirre, J. et al. The potential of photoacoustic microscopy as a tool to characterize the *in vivo* degradation of surgical sutures. *Biomed. Opt. Exp.* **5**, 2856–2869 (2014).
134. Nam, S. Y., Chung, E., Suggs, L. J. & Emelianov, S. Y. Combined ultrasound and photoacoustic imaging to noninvasively assess burn injury and selectively monitor a regenerative tissue-engineered construct. *Tissue Eng. Part C Me.* **21**, 557–566 (2015).
135. Aizawa, K., Sato, S., Saitoh, D., Ashida, H. & Obara, M. Photoacoustic monitoring of burn healing process in rats. *J. Biomed. Opt.* **13**, 064020 (2008).
136. Ida, T. et al. Real-time photoacoustic imaging system for burn diagnosis. *J. Biomed. Opt.* **19**, 086013 (2014).
137. Zhou, Y., Xing, W., Maslov, K. I., Cornelius, L. A. & Wang, L. V. Handheld photoacoustic microscopy to detect melanoma depth *in vivo*. *Opt. Lett.* **39**, 4731–4734 (2014).
138. Zhou, Y. et al. Handheld photoacoustic probe to detect both melanoma depth and volume at high speed *in vivo*. *J. Biophoton.* **8**, 961–967 (2015).
139. Welzel, J., Lankenau, E., Birngruber, R. & Engelhardt, R. Optical coherence tomography of the human skin. *J. Am. Acad. Dermatol.* **37**, 958–963 (1997).
140. Welzel, J. Optical coherence tomography in dermatology: a review. *Skin Re. Technol.* **7**, 1–9 (2001).
141. Zhao, Y. et al. Phase-resolved optical coherence tomography and optical Doppler tomography for imaging blood flow in human skin with fast scanning speed and high velocity sensitivity. *Opt. Lett.* **25**, 114–116 (2000).
142. Vogt, M. & Ermert, H. Development and evaluation of a high-frequency ultrasound-based system for *in vivo* strain imaging of the skin. *IEEE T. Ultrason. Ferr.* **52**, 375–385 (2005).
143. Turnbull, D. H. et al. A 40–100 MHz B-scan ultrasound backscatter microscope for skin imaging. *Ultrasound Med. Biol.* **21**, 79–88 (1995).
144. Serup, J., Keiding, J., Fullerton, A., Gniadecka, M. & Gniadecki, R. in *Handbook of non-invasive methods and the skin*. (eds Serup, J., Jemec, G. B. E. & Grove, G. L.) 473–491 (Taylor & Francis, 2006).
145. Mintz, G. S. et al. American College of Cardiology clinical expert consensus document on standards for acquisition, measurement and reporting of intravascular ultrasound studies (IVUS). *J. Am. Coll. Cardiol.* **37**, 1478–1492 (2001).
146. Nair, A. et al. Coronary plaque classification with intravascular ultrasound radiofrequency data analysis. *Circulation* **106**, 2200–2206 (2002).
147. Jang, I.-K. et al. Visualization of coronary atherosclerotic plaques in patients using optical coherence tomography: comparison with intravascular ultrasound. *J. Am. Coll. Cardiol.* **39**, 604–609 (2002).
148. VanderLaan, D., Karpouli, A. B., Yeager, D. & Emelianov, S. Real-time intravascular ultrasound and photoacoustic imaging. *IEEE T. Ultrason. Ferr.* **64**, 141–149 (2017).
149. Jansen, K. et al. Spectroscopic intravascular photoacoustic imaging of lipids in atherosclerosis. *J. Biomed. Opt.* **19**, 026006 (2014).
150. Wang, P. et al. High-speed intravascular photoacoustic imaging of lipid-laden atherosclerotic plaque enabled by a 2-kHz barium nitrite raman laser. *Sci. Rep.* **4**, 6889 (2014).
151. Jansen, K., Wu, M., van der Steen, A. F. & van Soest, G. Lipid detection in atherosclerotic human coronaries by spectroscopic intravascular photoacoustic imaging. *Opt. Exp.* **21**, 21472–21484 (2013).
152. Wang, B. et al. *In vivo* intravascular ultrasound-guided photoacoustic imaging of lipid in plaques using an animal model of atherosclerosis. *Ultrasound Med. Biol.* **38**, 2098–2103 (2012).
153. Zhang, J., Yang, S., Ji, X., Zhou, Q. & Xing, D. Characterization of lipid-rich aortic plaques by intravascular photoacoustic tomography. *J. Am. Coll. Cardiol.* **64**, 385–390 (2014).
154. Hui, J. et al. Real-time intravascular photoacoustic-ultrasound imaging of lipid-laden plaque in human coronary artery at 16 frames per second. *Sci. Rep.* **7**, 1417 (2017).
155. Ansari, R., Beard, P. C., Zhang, E. Z. & Desjardins, A. E. Photoacoustic endoscopy probe using a coherent fibre-optic bundle and Fabry-Pérot ultrasound sensor. In *Proc. SPIE 9708 Photons Plus Ultrasound: Imaging and Sensing* <https://doi.org/10.1117/12.2209687> (2016).
156. He, H., Wissmeyer, G., Ovsipian, S. V., Buehler, A. & Ntziachristos, V. Hybrid optical and acoustic resolution optoacoustic endoscopy. *Optics Letters* **41**, 2708–2710 (2016).
157. Yang, J.-M. et al. Simultaneous functional photoacoustic and ultrasonic endoscopy of internal organs *in vivo*. *Nat. Med.* **18**, 1297–1302 (2012).
158. Yang, J. M. et al. Three-dimensional photoacoustic endoscopic imaging of the rabbit esophagus. *PLoS ONE* **10**, e0120269 (2015).
159. Yang, J.-M. et al. Photoacoustic endoscopy. *Opt. Lett.* **34**, 1591–1593 (2009).
160. He, H., Buehler, A. & Ntziachristos, V. Optoacoustic endoscopy with curved scanning. *Opt. Lett.* **40**, 4667–4670 (2015).
161. Chen, S.-L., Ling, T., Baac, H. W. & Guo, L. J. Photoacoustic endoscopy using polymer microring resonators. In *Proc. SPIE 7899, Photons Plus Ultrasound: Imaging and Sensing* <https://doi.org/10.1117/12.874205> (2011).
162. Yuan, Y., Yang, S. & Xing, D. Preclinical photoacoustic imaging endoscope based on acousto-optic coaxial system using ring transducer array. *Opt. Lett.* **35**, 2266–2268 (2010).
163. Barendse, R. et al. Endoscopic mucosal resection vs transanal endoscopic microsurgery for the treatment of large rectal adenomas. *Colorectal Dis.* **14**, 191–196 (2012).
164. Soetikno, R. M., Gotoda, T., Nakanishi, Y. & Soehendra, N. Endoscopic mucosal resection. *Gastrointest. Endosc.* **57**, 567–579 (2003).
165. Yang, Y. et al. Integrated optical coherence tomography, ultrasound and photoacoustic imaging for ovarian tissue characterization. *Biomed. Opt. Exp.* **2**, 2551–2561 (2011).

166. Omar, M., Schwarz, M., Soliman, D., Symvoulidis, P. & Ntziachristos, V. Pushing the optical imaging limits of cancer with multi-frequency-band raster-scan optoacoustic mesoscopy (RSOM). *Neoplasia* **17**, 208–214 (2015).
167. Chekkoury, A. et al. High-resolution multispectral optoacoustic tomography of the vascularization and constitutive hypoxemia of cancerous tumors. *Neoplasia* **18**, 459–467 (2016).
168. Ellenbroek, S. I. & Van Rheenen, J. Imaging hallmarks of cancer in living mice. *Nat. Rev. Cancer* **14**, 406–418 (2014).
169. Kim, C. et al. *In vivo* molecular photoacoustic tomography of melanomas targeted by bioconjugated gold nanocages. *ACS Nano* **4**, 4559–4564 (2010).
170. Deán-Ben, X. L. et al. Functional optoacoustic neuro-tomography for scalable whole-brain monitoring of calcium indicators. *Light Sci. Appl.* **5**, e16201 (2016).
171. Deán-Ben, X. L. & Razansky, D. Adding fifth dimension to optoacoustic imaging: volumetric time-resolved spectrally enriched tomography. *Light Sci. Appl.* **3**, e137 (2014).
172. Stein, E. W., Maslov, K. & Wang, L. V. Noninvasive, *in vivo* imaging of blood-oxygenation dynamics within the mouse brain using photoacoustic microscopy. *J. Biomed. Opt.* **14**, 020502 (2009).
173. Stein, E. W., Maslov, K. & Wang, L. V. Noninvasive, *in vivo* imaging of the mouse brain using photoacoustic microscopy. *J. Appl. Phys.* **105**, 102027 (2009).
174. Johannes Rebling, J., Estrada, H., Zwack, M., Sela, G., Gottschalk, S., and Razansky, D., Hybrid ultrasound and dual-wavelength optoacoustic biomicroscopy for functional neuroimaging. In *Proc. SPIE 10064, Photons Plus Ultrasound: Imaging and Sensing* <https://doi.org/10.1117/12.2250635> (2017).
175. Estrada, H., Turner, J., Kneipp, M. & Razansky, D. Real-time optoacoustic brain microscopy with hybrid optical and acoustic resolution. *Laser Phys. Lett.* **11**, 045601 (2014).
176. Liao, L.-D. et al. Imaging brain hemodynamic changes during rat forepaw electrical stimulation using functional photoacoustic microscopy. *Neuroimage* **52**, 562–570 (2010).
177. Liao, L.-D. et al. Transcranial imaging of functional cerebral hemodynamic changes in single blood vessels using *in vivo* photoacoustic microscopy. *J. Cerebr. Blood F. Met.* **32**, 938–951 (2012).
178. Deng, Z., Wang, Z., Yang, X., Luo, Q. & Gong, H. *In vivo* imaging of hemodynamics and oxygen metabolism in acute focal cerebral ischemic rats with laser speckle imaging and functional photoacoustic microscopy. *J. Biomed. Opt.* **17**, 081415 (2012).
179. Yao, J. & Wang, L. V. Photoacoustic brain imaging: from microscopic to macroscopic scales. *Neurophotonics* **1**, 011003–011003 (2014).
180. Wang, D., Wu, Y. & Xia, J. Review on photoacoustic imaging of the brain using nanoprobe. *Neurophotonics* **3**, 010901–010901 (2016).
181. Hu, S. Listening to the brain with photoacoustics. *IEEE J. Sel. T. Quant.* **22**, 117–126 (2016).
182. Kim, K. et al. Photoacoustic imaging of early inflammatory response using gold nanorods. *Appl. Phys. Lett.* **90**, 223901 (2007).
183. Ha, S., Carson, A., Agarwal, A., Kotov, N. A. & Kim, K. Detection and monitoring of the multiple inflammatory responses by photoacoustic molecular imaging using selectively targeted gold nanorods. *Biomed. Opt. Exp.* **2**, 645–657 (2011).
184. Seeger, M., Karlas, A., Soliman, D., Pelisek, J. & Ntziachristos, V. Multimodal optoacoustic and multiphoton microscopy of human carotid atheroma. *Photoacoustics* **4**, 102–111 (2016).
185. Estrada, H., Sobol, E., Baum, O. & Razansky, D. Hybrid optoacoustic and ultrasound biomicroscopy monitors' laser-induced tissue modifications and magnetite nanoparticle impregnation. *Laser Phys. Lett.* **11**, 125601 (2014).
186. Lin, H. C. A. et al. Selective plane illumination optical and optoacoustic microscopy for postembryonic imaging. *Laser Photon. Rev.* **9**, 29–34 (2015).
187. Soliman, D., Tserevelakis, G. J., Omar, M. & Ntziachristos, V. Combining microscopy with mesoscopy using optical and optoacoustic label-free modes. *Sci. Rep.* **5**, 12902 (2015).
188. Tserevelakis, G. J., Soliman, D., Omar, M. & Ntziachristos, V. Hybrid multiphoton and optoacoustic microscope. *Opt. Lett.* **39**, 1819–1822 (2014).
189. Li, G., Li, L., Zhu, L., Xia, J. & Wang, L. V. Multiview Hilbert transformation for full-view photoacoustic computed tomography using a linear array. *J. Biomed. Opt.* **20**, 066010 (2015).
190. Harrison, T. et al. Combined photoacoustic and ultrasound biomicroscopy. *Opt. Exp.* **17**, 22041–22046 (2009).
191. Xi, L., Zhou, L. & Jiang, H. C-scan photoacoustic microscopy for *in vivo* imaging of *Drosophila* pupae. *Appl. Phys. Lett.* **101**, 013702 (2012).
192. Xie, B. et al. Optoacoustic detection of early therapy-induced tumor cell death using a targeted imaging agent. *Clin. Cancer Res.* **23**, 6893–6903 (2017).
193. Tomaszewski, M. R. et al. Oxygen enhanced optoacoustic tomography (OE-OT) reveals vascular dynamics in murine models of prostate cancer. *Theranostics* **7**, 2900 (2017).
194. Jose, J. et al. Initial results of imaging melanoma metastasis in resected human lymph nodes using photoacoustic computed tomography. *J. Biomed. Opt.* **16**, 096021 (2011).
195. Pramanik, M., Ku, G., Li, C. & Wang, L. V. Design and evaluation of a novel breast cancer detection system combining both thermoacoustic (TA) and photoacoustic (PA) tomography. *Med. Phys.* **35**, 2218–2223 (2008).
196. Kolkman, R. G. M. et al. Photoacoustic mammography laboratory prototype: imaging of breast tissue phantoms. *J. Biomed. Opt.* **9**, 1172 (2004).
197. Jose, J., Manohar, S., Kolkman, R. G., Steenbergen, W. & van Leeuwen, T. G. Imaging of tumor vasculature using Twente photoacoustic systems. *J. Biophoton.* **2**, 701–717 (2009).
198. Heijblom, M. et al. Imaging tumor vascularization for detection and diagnosis of breast cancer. *Technol. Cancer Res. T.* **10**, 607–623 (2011).
199. Heijblom, M. et al. Visualizing breast cancer using the Twente photoacoustic mammoscope: what do we learn from twelve new patient measurements? *Opt. Exp.* **20**, 11582–11597 (2012).
200. Gurka, M. K. et al. Identification of pancreatic tumors *in vivo* with ligand-targeted, pH responsive mesoporous silica nanoparticles by multispectral optoacoustic tomography. *J. Control. Release* **231**, 60–67 (2016).
201. Valluru, K. S. & Willmann, J. K. Clinical photoacoustic imaging of cancer. *Ultrasound* **35**, 267 (2016).
202. Stoffels, I. et al. Metastatic status of sentinel lymph nodes in melanoma determined noninvasively with multispectral optoacoustic imaging. *Sci. Transl. Med.* **7**, 317ra199 (2015).
203. Neuschmelting, V., Lockau, H., Ntziachristos, V., Grimm, J. & Kircher, M. F. Lymph node micrometastases and in-transit metastases from melanoma: *in vivo* detection with multispectral optoacoustic imaging in a mouse model. *Radiology* **280**, 137–150 (2016).
204. Waldner, M. J. et al. Multispectral optoacoustic tomography in Crohn's disease: noninvasive imaging of disease activity. *Gastroenterology* **151**, 238–240 (2016).
205. Knieling, F. et al. Multispectral optoacoustic tomography in Crohn's disease — a first-in-human diagnostic clinical trial. *J. Nuclear Med.* **58**, 379–379 (2017).
206. Lev-Tov, H. Dive deep, stay focused! *Sci. Transl. Med.* **9**, eaan4292 (2017).
207. Allen, T. J., Hall, A., Dhillon, A. P., Owen, J. S. & Beard, P. C. Spectroscopic photoacoustic imaging of lipid-rich plaques in the human aorta in the 740 to 1400 nm wavelength range. *J. Biomed. Opt.* **17**, 061209 (2012).
208. Liotta, L. A., Steeg, P. S. & Stetler-Stevenson, W. G. Cancer metastasis and angiogenesis: an imbalance of positive and negative regulation. *Cell* **64**, 327–336 (1991).
209. Filonov, G. S. et al. Deep-tissue photoacoustic tomography of a genetically encoded near-infrared fluorescent probe. *Angew. Chem. Int. Ed.* **51**, 1448–1451 (2012).
210. Deán-Ben, X. L. & Razansky, D. Functional optoacoustic human angiography with handheld video rate three dimensional scanner. *Photoacoustics* **1**, 68–73 (2013).
211. Zabihian, B. et al. *In vivo* dual-modality photoacoustic and optical coherence tomography imaging of human dermatological pathologies. *Biomed. Opt. Exp.* **6**, 3163–3178 (2015).
212. Castelino, R. F., Hynes, M., Mundig, C. E., Telenkov, S. & Foster, F. S. Combined frequency domain photoacoustic and ultrasound imaging for intravascular applications. *Biomed. Opt. Exp.* **7**, 4441–4449 (2016).
213. Ji, X., Xiong, K., Yang, S. & Xing, D. Intravascular confocal photoacoustic endoscope with dual-element ultrasonic transducer. *Opt. Exp.* **23**, 9130–9136 (2015).
214. Jansen, K., Van der Steen, A. F., Van Beusekom, H. M., Oosterhuis, J. W. & Van Soest, G. Intravascular photoacoustic imaging of human coronary atherosclerosis. *Opt. Lett.* **36**, 597–599 (2011).
215. Karpouli, A. B., Wang, B. & Emelianov, S. Y. Development of a catheter for combined intravascular ultrasound and photoacoustic imaging. *Rev. Sci. Instrum.* **81**, 014901 (2010).
216. Yang, J.-M. et al. A 2.5-mm diameter probe for photoacoustic and ultrasonic endoscopy. *Opt. Exp.* **20**, 23944–23953 (2012).
217. Subochev, P. et al. Simultaneous photoacoustic and optically mediated ultrasound microscopy: phantom study. *Opt. Lett.* **37**, 4606–4608 (2012).
218. Subochev, P., Orlova, A., Shirmanova, M., Postnikova, A. & Turchin, I. Simultaneous photoacoustic and optically mediated ultrasound microscopy: an *in vivo* study. *Biomed. Opt. Exp.* **6**, 631–638 (2015).
219. Subochev, P., Fiks, I. & Frenz, M. Simultaneous triple-modality imaging of diffuse reflectance, optoacoustic pressure and ultrasonic scattering using an acoustic-resolution photoacoustic microscope: feasibility study. *Laser Phys. Lett.* **13**, 025605 (2016).

220. Subochev, P. Cost-effective imaging of optoacoustic pressure, ultrasonic scattering, and optical diffuse reflectance with improved resolution and speed. *Opt. Lett.* **41**, 1006–1009 (2016).
221. Liu, M. et al. *In vivo* three dimensional dual wavelength photoacoustic tomography imaging of the far-red fluorescent protein E2-Crimson expressed in adult zebrafish. *Biomed. Opt. Exp.* **4**, 1846–1855 (2013).

Acknowledgements

The authors would like to thank Chapin Rodriguez for proofreading the manuscript and for his valuable suggestions, and Luis Den Bean for his useful comments and suggestions. V.N. acknowledges funding from the Deutsche Forschungsgemeinschaft, Germany (Leibniz Prize 2013; NT 3/10-1), from the European Union's Horizon 2020 research and innovation programme under grant agreement No 687866 (INNODERM), and from the European Union's Horizon 2020 research and innovation programme under grant agreement No 732720 (ESOTRAC). The content of this manuscript reflects only the authors' view, and the European commission is not responsible for any use that may be made of the information provided.

Author contributions

All authors contributed to writing the paper, revising it and approving the final version.

Competing interests

V.N. is a shareholder in iThera Medical GmbH, a company that commercializes photoacoustic mesoscopy. The company did not provide support for this work.

Additional information

Supplementary information is available for this paper at <https://doi.org/10.1038/s41551-019-0377-4>.

Reprints and permissions information is available at www.nature.com/reprints.

Correspondence should be addressed to V.N.

Publisher's note: Springer Nature remains neutral with regard to jurisdictional claims in published maps and institutional affiliations.

© Springer Nature Limited 2019